Journal of Controlled Release 389 (2026) 114469

Contents lists available at ScienceDirect

Journal of Controlled Release

journal homepage: www.elsevier.com/locate/jconrel

Bilayer gelatin-methacryloyl scaffold for pulp inflammation suppression and dentin-like tissue regeneration

Caroline Anselmi [a,b], Renan Dal-Fabbro [a], Hisham Abada [a,c], Igor Paulino Mendes Soares [a,d], Lais M. Cardoso [a,d], Abdel H. Mahmoud [a], Julia C. Catalano [e], Ana Beatriz Gomes de Carvalho [a], Yuanyuan Han [a], Prabaha Sikder [f], Anna Schwendeman [e], Josimeri Hebling [b], Marco C. Bottino [a,g,*]

[a] Department of Cariology, Restorative Sciences and Endodontics, University of Michigan School of Dentistry, Ann Arbor, MI, USA
[b] Department of Morphology, Genetics, Orthodontics and Pediatric Dentistry, School of Dentistry, São Paulo State University, Araraquara, Brazil
[c] Department of Endodontics, Faculty of Dentistry, Kafrelsheikh University, Kafrelsheikh, Egypt
[d] Department of Dental Materials and Prosthodontics, School of Dentistry, São Paulo State University, Araraquara, Brazil
[e] Department of Pharmaceutical Sciences, University of Michigan, Ann Arbor, MI, USA
[f] Department of Mechanical Engineering, Cleveland State University, Cleveland, OH, USA
[g] Department of Biomedical Engineering, University of Michigan, Ann Arbor, MI, USA

ARTICLE INFO

Keywords:
Polymer nanofibers
Gelatin methacryloyl
Regeneration
Mineralized tissue
Dental pulp
Dentistry
Pulp capping

ABSTRACT

Balancing pulp tissue inflammation and dentin regeneration is essential for maintaining tooth responsiveness and reparative ability in vital pulp therapy (VPT). Here, we describe a photocrosslinkable gelatin methacryloyl (GelMA) biomaterial electrospun into a bilayer fibrous scaffold with clinically relevant functions. It comprises a 10 % (*w/v*) GelMA layer loaded with ibuprofen (IBP, 10 % or 20 % *w*/w) for immunomodulation, and a 20 % GelMA layer containing amorphous magnesium phosphate (AMP, 5 % or 15 % w/w) to promote biomineralization. Fiber morphology, chemical composition, mechanical properties, swelling, enzymatic degradation, and release kinetics of IBP and Mg^{2+}/PO_4^{3-} ions were evaluated. Bioactivity was assessed with human dental pulp stem cells (DPSCs), macrophages, an LPS-challenged artificial pulp chamber (APC) model, and subcutaneous implantation. All fibers were bead-free and porous, and photocrosslinking yielded pulp-like stiffness. IBP-loaded fibers showed an initial burst followed by sustained release over 14 days; AMP fibers released ions continuously for 7 days. IBP layer reduced IL-1α, TNF-α, and IL-6 secretion, inhibiting NF-κB activation without cytotoxicity. AMP layer increased ALP activity, mineral deposition, and expression of *COL1A1*, *RUNX2*, and *ALPL*. In the APC model, the bilayer scaffold downregulated *IL1A*, *IL1B*, and *TNF* within 3 h; after 14 days, it upregulated *ALPL*, *DSPP*, and *OCN* compared to controls under LPS. Subcutaneous implantation confirmed biocompatibility: IBP decreased M1 polarization, while AMP induced transient RUNX-2 followed by ALP and osteocalcin, indicating ongoing mineralization. The dual functionality of this bilayer scaffold suggests it may serve as a promising next-generation VPT biomaterial capable of controlling inflammation and guiding dentin-like tissue regeneration.

1. Introduction

Pulpitis is often caused by the diffusion of bacteria and their metabolites through the dentinal tubules into the pulp space as carious lesions progress [1]. Initially, inflammatory mediators stimulate dentinogenesis by recruiting underlying odontoblasts and mesenchymal stem cells to replace lost odontoblasts, thereby restoring the dynamics of the dentin-pulp complex [1]. However, if inflammation is not suppressed, the pulp tissue will degenerate and must be removed [1]. Vital pulp therapy (VPT) represents the proper balance between inflammation and dentin regeneration [2], potentially preserving the tooth's intrinsic responsiveness and reparative mechanisms, while avoiding the disadvantages of conventional root canal therapy (*e.g.*, tooth brittleness, discoloration, and reinfection) [2].

* Corresponding author at: University of Michigan School of Dentistry, Department of Cariology, Restorative Sciences, and Endodontics, Department of Biomedical Engineering, College of Engineering, University of Michigan, 1011 N. University (Room 2303), Ann Arbor, MI 48109, USA.
E-mail address: mbottino@umich.edu (M.C. Bottino).

https://doi.org/10.1016/j.jconrel.2025.114469
Received 10 September 2025; Received in revised form 21 November 2025; Accepted 24 November 2025
Available online 25 November 2025

Calcium hydroxide and calcium silicate formulations are currently available for VPT, with high clinical success rates [3,4]. Despite their undeniable ability to induce tertiary dentin deposition, mostly by dystrophic calcification, these materials cannot resolve pulp tissue inflammation [5,6], limiting their current application to asymptomatic, reversible pulpitis conditions only. However, given the intrinsic regenerative potential of the pulp, VPT could be considered as a treatment independent of a diagnosis of reversible or irreversible pulpitis [7]. Therefore, next-generation materials for VPT should leverage biomaterial-driven therapeutic platforms that can rapidly suppress inflammation and stimulate dentin-like tissue deposition by progenitor cells [8].

Polymeric nanofibers offer a highly biomimetic pulp-like native architecture that facilitates cell adhesion, proliferation, and differentiation [9]. Gelatin methacryloyl (GelMA) has been highlighted as a versatile material for tissue regeneration in inflammatory environments, as it degrades when exposed to matrix metalloproteinases, effectively releasing entrapped therapeutic cargo [10]. Reports show that photocrosslinkable GelMA nanofibers have been investigated for bone regeneration and the prevention of microbial infections [11,12]. For VPT, beta-tricalcium phosphate-laden GelMA fibers supported odontogenic differentiation of human dental pulp stem cells (DPSCs) and mineralized tissue formation *in vivo* [13].

Given the slow resorption of traditional calcium phosphates (*e.g.*, hydroxyapatite), exploring novel bioceramic alternatives may lead to enhanced mineralization outcomes [14]. Notably, recent studies have highlighted the use of magnesium (Mg^{2+}) as a substitute for calcium (Ca^{2+}) due to its higher biodegradability [15,16]. Indeed, amorphous magnesium phosphate (AMP) has been shown to induce pre-osteoblast differentiation and enhance osteoclast and osteoblast metabolism due to its high solubility and local Mg^{2+} release [17]. Meanwhile, AMP presentation within bioprinted extracellular matrix-based hydrogel constructs laden with DPSCs results in enhanced mineralized matrix secretion [18]. Therefore, in this study, we first tested the hypothesis that incorporating AMP into GelMA fibers would benefit DPSC differentiation, promoting dentin-like tissue regeneration.

Due to its low cost and easy availability, Ibuprofen (IBP) is one of the most widely used nonsteroidal anti-inflammatory drugs. Clinically, IBP has been shown to decrease levels of the proinflammatory cytokines PGE-2, IL-6, TNF-α, and IFN-γ in human dental pulp when taken orally in teeth with irreversible pulpitis [19]. However, there is evidence that IBP can increase the stemness of DPSCs and decrease the mineralization potential of mesenchymal stem cells in a dose-dependent manner [20,21]. Therefore, our second hypothesis was that incorporating IBP into GelMA fibers would effectively reduce the levels of inflammatory mediators. [22]. Based on its clinical anti-inflammatory effect but recognizing its potential to reduce stem cell mineralization in a dose-dependent manner, we hypothesized that incorporating IBP into GelMA fibers could attenuate inflammatory mediators while maintaining DPSC viability. In parallel, AMP incorporation was expected to enhance odontogenic differentiation. Therefore, we designed a bilayer scaffold combining both strategies to address inflammation and regeneration simultaneously.

2. Materials and methods

2.1. Fabrication of photocrosslinkable GelMA fibers containing IBP or AMP

GelMA was synthesized from Type-A Gelatin derived from porcine skin (SLBM9945V, Sigma-Aldrich, St. Louis, MO, USA). Initially, type-A Gelatin was dissolved (10 %; *w/v*) in Dulbecco's phosphate-buffered saline (DPBS, 14190144, Thermo Fisher Scientific, Waltham, MA, USA). Following that, methacrylic anhydride (8 mL) was added to the dissolved gel using an automatic pump (0.5 mL/min) under stirring conditions at 60 °C. It was allowed to react for 2 h. The reaction was stopped by doubling the amount of DPBS in the solution. Lastly, the mixture was dialyzed in deionized water to remove any unreacted monomers using a 12–14 kDa dialysis tube at 45 ± 5 °C for 7 days, refreshed twice daily. The prepared solution was frozen at −80 °C for at least 2 days and then lyophilized (Labconco FreeZone 2.5 L, Labconco Corporation, Kansas City, MO, USA) for 7 days.

Next, we fabricated electrospun fibers composed of GelMA loaded with either IBP or AMP. Two concentrations of GelMA were established: 10 % (*w/v*) for IBP-loaded fibers and 20 % (w/v) for AMP-incorporated fibers based on their faster and slower degradation profiles, respectively. Our lyophilized GelMA was dissolved in acetic acid under continuous stirring at 60 °C for 12 h. After complete dissolution, IBP was added at concentrations of 0 %, 10 %, and 20 % (*w*/w), and AMP was added at concentrations of 0 %, 5 %, and 15 % (w/w), followed by additional stirring. Approximately 1 h before electrospinning, lithium phenyl-2,4,6-trimethylbenzoylphosphinate (LAP, TCI America Inc., Portland, OR, USA) was added as a photoinitiator at a final concentration of 0.075 % (*w/v*). Electrospinning was conducted using a 27-gauge needle with an applied voltage of 18–20 kV, a flow rate of 1.3–1.8 mL/h, and a distance of 14 cm between the needle and the rotating collector (120–160 rpm).

2.1.1. Morphological and chemical characterization of the processed fibers

The morphological characterization of the individual electrospun fibrous layers was performed using scanning electron microscopy (SEM; TESCAN MIRA3 FEG-SEM, Brno, Czech Republic). For this, six specimens (10 × 10 mm^2) were prepared for each group (GelMA 10 %, GelMA 10 % + 10 % IBP, GelMA 10 % + 20 % IBP, GelMA 20 %, GelMA 20 % + 5 % AMP, and GelMA 20 % + 15 % AMP). Three specimens from each group were submitted to the photocrosslinking process (crosslinked fibers), while the others remained uncrosslinked. The samples were then mounted on aluminum stubs, sputter-coated with gold, and scanned at 5000× magnification. We analyzed fiber diameter and frequency distribution using the ImageJ software (National Institute of Health, NIH, Bethesda, MD, USA) by measuring 50 fibers across the three distinct fibrous layers (total number of fibers = 150) [23].

The GelMA-based fibers incorporated with AMP were subjected to elemental composition analysis using Energy-dispersive X-ray spectroscopy (EDS) coupled with SEM, generating elemental mapping images and the mass percentage of each detected element (Kratos Analytical Ltd., Axis Ultra XPS, Shimadzu Corporation, Manchester, UK) [13]. The chemical characterization of all formulated fibers was assessed by Fourier Transform Infrared Spectroscopy (FTIR) (ATR-FTIR, Nicolet iS50, Thermo Fisher Scientific). Three samples of each group (10 × 10 mm^2) were prepared, crosslinked, and evaluated regarding their composition. The spectra of each group, along with as-received IBP and AMP powders, were obtained within a spectral range of 4000–400 cm^{-1}, with a resolution of 4 cm^{-1} and 16 scans [23].

2.1.2. Mechanical characterization

To assess the mechanical properties of all electrospun fibers, including the bilayer formulation (GelMA 10 % + 10 % IBP / GelMA 20 % + 5 % AMP), rectangular samples (25 mm × 3 mm, $n = 6$/group) were prepared and subjected to photocrosslinking. Their thickness was then measured at three different locations using a digital caliper (Mitutoyo Digimatic Caliper; Mitutoyo Corporation, Tokyo, Japan) to obtain an average thickness. Uniaxial tensile testing was then carried out using an eXpert 5601 machine (ADMET, Inc., Norwood, MA, USA) at a crosshead speed of 1 mm/min to determine Young's modulus (kPa), elongation at break (%), and tensile strength (kPa) [13].

2.1.3. Swelling ratio and degradation profile

All electrospun fibers were cut (10 × 10 mm^2, $n = 6$/group), crosslinked, and their initial weight (W_0) was obtained. Subsequently, the samples were placed in vials containing 2 mL of PBS (Gibco, Carlsbad, CA, USA), followed by incubation at 37 °C in a Heratherm Incubator

IGS60 (Thermo Fisher Scientific, Waltham, MA, USA). At predefined time-points (1, 3, 6, and 24 h), the samples were removed, gently blotted using low-lint Kimwipes papers (Kimberly-Clark, Irving, TX, USA), and reweighed (W_t). The swelling ratio was calculated using the following equation [13]:

$$\text{Swelling } (\%) = [(W_t - W_o)/W_o] \times 100$$

For the degradation profile analysis, fibers of the distinct compositions ($n = 3$/group) were prepared as previously described, and their initial weight (W_o) was recorded before placing the samples in vials containing 2 mL of collagenase type A solution (1 U/mL; Collagenase from *Clostridium histolyticum*, Sigma-Aldrich) in PBS (Gibco). The vials were incubated at 37 °C (Heratherm Incubator IGS60) for up to 21 days, with the collagenase solution refreshed every 48 h. At predefined time-points, the samples were washed twice with distilled water, dried in a vacuum oven (Isotemp Vacuum Oven Model 281 A, Thermo Fisher Scientific) at room temperature for 24 h, and reweighed (W_t). The degradation ratio was calculated using the following equation: Remaining mass (%) = (W_t / W_o) × 100 [13].

2.1.4. Ibuprofen and ion release analysis

We employed ultra-performance liquid chromatography (UPLC) to quantify the release of ibuprofen from GelMA/ibuprofen electrospun fibrous layers ($n = 3$/group) immersed in PBS (Gibco) at 37 °C. After 12 h, 24 h, 48 h, 72 h, 7 days, and 14 days, samples were vortexed, and the supernatants were collected and stored at −20 °C until the analysis. Analyses were carried out using a Waters Acquity UPLC BEH C18 column (1.7 μm, 2.1 × 50 mm) maintained at room temperature. The mobile phase consisted of a 100 mM phosphate buffer (pH 6.8) and acetonitrile mixed in a 65:35 (*v*/v) ratio, delivered at a flow rate of 0.5 mL/min. A 2 μL injection volume was used for each sample. The fluorescence was detected at an excitation wavelength of 227 nm and an emission wavelength of 276 nm. The total run time was 6 min. Before analysis, samples were diluted in the mobile phase and filtered through a 0.22 μm PVDF syringe filter. To ensure measurements remained within the linear range of detection, samples were diluted by factors of 5, 10, 50, 100, or 200, as appropriate.

The ion release of magnesium (Mg) and phosphate (PO) was analyzed using inductively coupled plasma mass spectrometry (ICP-MS). Electrospun fibers (10 × 10 mm^2), incorporated or not with AMP (GelMA 20 %, GelMA 20 % + 5 % AMP, and GelMA 20 % + 15 % AMP), were immersed in ultrapure water (Invitrogen, Carlsbad, CA, USA) at 37 °C. After 1, 3, and 7 days, the samples were vortexed, the total supernatant was collected, and water was added to maintain a constant volume of 1 mL. The collected supernatants were filtered through a 0.22 μm filter, diluted 1:500 to match the detection limits, and analyzed using a NexION 300D ICP-MS (PerkinElmer, USA). The concentrations of ions were determined using standardized calibration curves from standard solutions. Internal standards (bismuth and yttrium) were used to correct for matrix effects. Six replicates per sample were analyzed and averaged. The results were reported in parts per billion (ppb) as mean ± 95 % confidence interval (CI).

2.2. In vitro cytocompatibility and bioactivity studies

2.2.1. Dental pulp stem cells – electrospun fibers interaction

Dental pulp stem cells (DPSCs; Lonza; #PT-5025, Walkersville, MD, USA) were cultured in complete minimum essential alpha medium (α-MEM; Gibco, Carlsbad, CA, USA) supplemented with 15 % fetal bovine serum (FBS; Gibco) and 1 % penicillin/streptomycin (Gibco). DPSCs at passages 4–8 were used for all experiments. The response of DPSCs to direct contact with each electrospun fibrous layer was assessed individually. Before cell seeding, fibrous layers corresponding to each formulation were placed in 24-well plates (Corning, New York, NY, USA) and disinfected with UV light for 1 h on each side. Samples were then soaked in 70 % ethanol for 10 min, rinsed twice with PBS for 5 min, and incubated in complete α-MEM for 1 h. A single 20 μL drop of cell suspension was placed in the center of each sample, with the cell density adjusted according to the protocol described below.

2.2.2. DPSCs spreading, adhesion, and morphology

DPSCs (3×10^4) were cultured on the electrospun fibrous layers for 1, 3, 5, and 7 days in complete α-MEM. At each time point, cell-laden constructs ($n = 2$) were fixed with 4 % buffered paraformaldehyde, stained with a green fluorescence probe for actin filaments (1:20 in PBS; ActinGreen 488 ReadyProbes; Invitrogen, Carlsbad, CA, USA), and counterstained with DAPI (1:5000 in PBS; Invitrogen) for nuclei visualization. We used a fluorescence microscope (Echo Revolve, BICO Company, San Diego, CA, USA) to qualitatively analyze DPSC spreading and adhesion on the electrospun fibers. Additionally, cell morphology was evaluated after 1 and 3 days of culture. Briefly, following a PBS wash, cells were fixed with 2.5 % glutaraldehyde and then dehydrated using a graded ethanol series (30 %, 50 %, 70 %, 90 %, and absolute ethanol). Final drying was achieved by overnight incubation with hexamethyldisilazane. The morphology of DPSCs on the electrospun fibrous layers was then examined using a field emission scanning electron microscope (SEM, MIRA3, TESCAN Brno, Kohoutovice, Czech Republic).

2.2.3. DPSCs viability and proliferation

DPSCs (3×10^4) were cultured on the electrospun fibrous layers in complete α-MEM. At 1, 3, 5, and 7 days, samples were incubated with a 10 % alamarBlue solution (Invitrogen) in FBS-free α-MEM for 3 h at 37 °C. The fluorescence of the supernatant was collected and measured at an excitation wavelength of 560 nm and an emission wavelength of 590 nm using a microplate reader (SpectraMax iD3, Molecular Devices LLC, San Jose, CA, USA). The mean fluorescence obtained for the GelMA 10 % electrospun fibers on day 1 was used as the reference, representing 100 % cell viability. Cell proliferation was indirectly assessed by comparing fluorescence values across different time points.

2.2.4. Anti-inflammatory effects of IBP-incorporated fibers on macrophages

The anti-inflammatory effects of the IBP-incorporated electrospun fibrous layer were tested using extracts collected from respective samples incubated for 24 h in FBS-free DMEM (Gibco). These extracts were then applied to RAW264.7 cells, which had been previously seeded (1×10^5) in 24-well plates with Dulbecco's Modified Eagle Medium (DMEM) containing 10 % FBS and stimulated with 0.1 μg/mL *E. coli* LPS (Lipopolysaccharide; serotype O111:B4, Sigma-Aldrich). After 24 h, the concentrations (pg/mL) of IL-1α, TNF-α, and IL-6 in the cell culture supernatants were determined using ELISA kits (#433404, #431304, and #430904, BioLegend, San Diego, CA, USA) according to the manufacturer's instructions. Additionally, the effects of the samples' extracts on the activation of the nuclear factor *kappa* B (NF-κB) signaling pathway were evaluated using NF-κB Luciferase Stable RAW264.7 cells (T3015, Applied Biological Materials Inc., Canada). These cells were seeded (0.75×10^5) in 96-well plates with DMEM containing 10 % FBS (Gibco) and then cultured with the samples' extracts in the presence of 0.1 μg/mL *E. coli* LPS (serotype O111:B4, Sigma-Aldrich). NF-κB activation was assessed 6 h after stimulation using a luciferase assay system (Promega Corporation, Madison, WA, USA), and luminescence intensity was measured (SpectraMax iD3). For both experiments, the negative control consisted of cells cultured in FBS-free DMEM without LPS, while the positive control included cells cultured in FBS-free DMEM with LPS.

2.2.5. Odontogenic differentiation induction of AMP-incorporated fibers on DPSCs

To quantify alkaline phosphatase (ALP) activity, DPSCs (5×10^5) were cultured on the electrospun fibers for 7 and 14 days. The cells were maintained either in complete α-MEM (used as basal medium) or in an osteogenic medium composed of α-MEM supplemented with 0.1 μM dexamethasone, 10 mM β-glycerophosphate, and 50 μg/mL ascorbic acid. At each time point, cell lysates were prepared using 300 μL of

Triton X-100. The lysates were then centrifuged at 2500 ×*g* for 10 min at 4 °C, and the resulting supernatants were collected for analysis of ALP activity. ALP quantification was performed using the SensoLyte pNPP ALP Assay Kit (AnaSpec Inc. & Eurogentec US, Fremont, CA, USA), according to the manufacturer's protocol. The reaction was initiated by adding pNPP substrate to the samples, and after incubation for 1 h, absorbance was measured at 405 nm (SpectraMax iD3). ALP concentrations were calculated based on a standard calibration curve and expressed in ng/mg of protein.

Mineralized matrix formation was assessed using Alizarin Red staining (40 mM, pH 4.2; Sigma-Aldrich). To do this, DPSCs (5×10^5) were seeded on the electrospun fibers and cultured under both basal and osteogenic conditions for 14 and 21 days. To quantify the mineral deposits, a 10 mM solution of cetylpyridinium chloride (pH 7.0; Sigma-Aldrich) was used to solubilize the stained nodules. The optical density of the extracted dye was measured at 560 nm (SpectraMax iD3). Absorbance data were expressed as a percentage of the control group (GelMA 20 %), which was set at 100 %. To normalize the results, electrospun fibers without cells, but maintained under identical culture conditions, were used as references.

For gene expression analysis, we used cells cultured under the same experimental conditions. Total RNA was isolated using TRIzol reagent and subsequently purified with an affinity column-based method, following the manufacturer's instructions (RNAqueous Micro Total Isolation Kit; Invitrogen). After purification, the quantity and purity of the RNA were assessed using spectrophotometric analysis. The 260/280 nm absorbance ratio served as a quality indicator (SpectraMax iD3). Complementary DNA (cDNA) synthesis was performed from 600 ng of RNA through reverse transcription, following the protocol provided with the SuperScript™ II Reverse Transcriptase kit (Applied Biosystems, Thermo Fisher Scientific, Foster City, CA, USA). Quantitative polymerase chain reaction (qPCR) was then carried out using 1 μL of cDNA per reaction, with primer-probe sets at optimized concentrations (TaqMan Gene Expression Assays; Applied Biosystems). The target genes amplified included *ALPL* (Hs01029144_m1), *COL1A1* (Hs00164004_m1), and *RUNX2* (Hs01047973_m1), while *GAPDH* (Hs02758991_g1) served as the reference gene. Expression levels were normalized to those of the control group treated with GelMA 20 %, and fold changes were calculated using the $2^{-\Delta\Delta Ct}$ method.

2.2.6. Effect of bilayer scaffolds on DPSCs in a simulated inflammatory environment

Artificial pulp chambers (APCs) containing three-dimensional cultures of DPSCs, stimulated with lipopolysaccharide (LPS), were used to simulate *in vitro* pulp exposure a clinical scenario of pulp exposure, as described elsewhere [24]. Briefly, dentin discs with a central perforation (0.5 × 7 mm) were placed between two silicone rings and mounted in stainless-steel APCs to ensure proper sealing (Institutional Review Board approval: HUM00154490, University of Michigan). DPSCs (1×10^5) were seeded in 3D collagen type I matrices (rat tail, 4.39 mg/mL; Corning, Discovery Labware Inc., Bedford, MA, USA) prepared with 10× α-MEM (5:1; GIBCO, Invitrogen) and neutralized using 5 M sodium hydroxide. To induce an inflammatory environment, cultures were treated with 10 μg/mL *E. coli* LPS (Sigma-Aldrich) for 3 days prior to APC assembly [25]. Following LPS treatment, the 3D cultures were positioned on the pulpal side of the dentin discs, and scaffolds (3 mm diameter) were placed over the perforation with the IBP-incorporated layer facing the DPSC culture. For gene expression analysis, scaffolds remained in contact with the 3D culture for either 3 h or 14 days. Culture media were changed every 2 days. RNA extraction, purification, and reverse transcription were performed as described in Section 2.2.5. Quantitative PCR (qPCR) was performed using TaqMan Gene Expression Assays (Applied Biosystems) with gene-specific primers and hydrolysis probes. Inflammatory markers *IL1A* (Hs00174092_m1), *IL1B* (Hs01555410_m1), and *TNF* (Hs00174128_m1) were evaluated after 3 h. After 14 days, dentin-pulp regeneration markers *ALPL* (Hs01029144_m1), *RUNX2* (Hs01047973_m1), *DSPP* (Hs00171962_m1), and *OCN* (Hs01587814_g1) were analyzed. Gene expression was normalized to *GAPDH* (Hs02758991_g1), and fold changes were calculated using the $2^{-\Delta\Delta Ct}$ method relative to the untreated control group.

2.3. In vivo subcutaneous model

Fifteen male Fischer 344 rats, 12 weeks old and weighing roughly 300 g, were obtained from Envigo RMS (Oxford, MI, USA) and randomly assigned to post-operative intervals of 7, 14, or 21 days (five animals per interval) under an approved Institutional Animal Care and Use Committee protocol (IACUC #PRO00012062). While under isoflurane anesthesia, each rat had its dorsal hair clipped and skin disinfected with povidone-iodine. Then, a 2 cm midline incision was made with a #15 blade, and blunt dissection then produced four subcutaneous pockets. Sterile 10 mm × 10 mm electrospun fibrous samples (GelMA 10 %, GelMA 10 % + 10 % IBP, GelMA 10 % + 20 % IBP, GelMA 20 %, or GelMA 20 % + 5 % AMP) were implanted according to a randomization scheme. This ensured that no single animal received more than one ibuprofen dose, thereby avoiding systemic crossover. Incisions were closed using coated Vicryl® (polyglactin-910) sutures (Ethicon Endo-Surgery, Cincinnati, OH). The rats were monitored until full recovery, and, at their designated time point, were humanely euthanized by CO_2 overdose [26,27].

Following euthanasia, retrieved specimens were immersed overnight in 10 % neutral-buffered formalin, processed for paraffin embedding, and sectioned at 5 μm. Hematoxylin and eosin staining was used to evaluate inflammatory infiltration and electrospun fiber degradation. Meanwhile, immunofluorescence was carried out with primary antibodies diluted 1:100 and incubated overnight at 4 °C: anti-osteocalcin (#23418–1-AP, Proteintech), anti-RUNX2 (#ab92336, Abcam), anti-alkaline phosphatase (#MA5–24845, Invitrogen) to monitor mineralization in AMP-laden fibers, and anti-iNOS (#ab283655, Abcam) plus anti-CD163 (#ab182422, Abcam) to probe macrophage polarization induced by IBP-loaded electrospun fibers. Secondary detection employed Goat Anti-Rabbit IgG conjugated to Alexa Fluor 488 (#ab150077, Abcam) for OCN, iNOS, and CD163, and Alexa Fluor 594 (#A-11012, Invitrogen) for RUNX2 and ALP, each at 1:100 for 2 h at room temperature; nuclei were counterstained with VECTASHIELD®-mounted DAPI. Images were acquired at 10× magnification using an ECHO Revolve microscope (BICO) and quantified in ImageJ by analyzing six randomly selected fields per group, separating the colour channels, and calculating the proportion of the field occupied by positive fluorescence [11,28].

2.4. Statistical analysis

Statistical analyses were performed using SPSS version 20.0 (IBM Corp., Chicago, IL, USA) and GraphPad Prism 10.0 software (GraphPad Software, Inc., San Diego, CA, USA), with a significance level of 5 %. The distribution of each dataset was assessed using the Shapiro–Wilk test, and homogeneity of variances was verified *via* the Levene test. Based on the number of independent variables, data were analyzed using either one-way or two-way ANOVA, followed by appropriate *post hoc* tests such as Tukey's, Games–Howell's, or Sidak's when indicated. Swelling, degradation, and drug release data were inferred using a 95 % confidence interval.

3. Results and discussion

3.1. Morphological, chemical, and mechanical characterizations

The morphological analysis of the electrospun fibers by SEM revealed a three-dimensional porous network with no beads and randomly oriented fibers for all formulations. The electrospun fibers

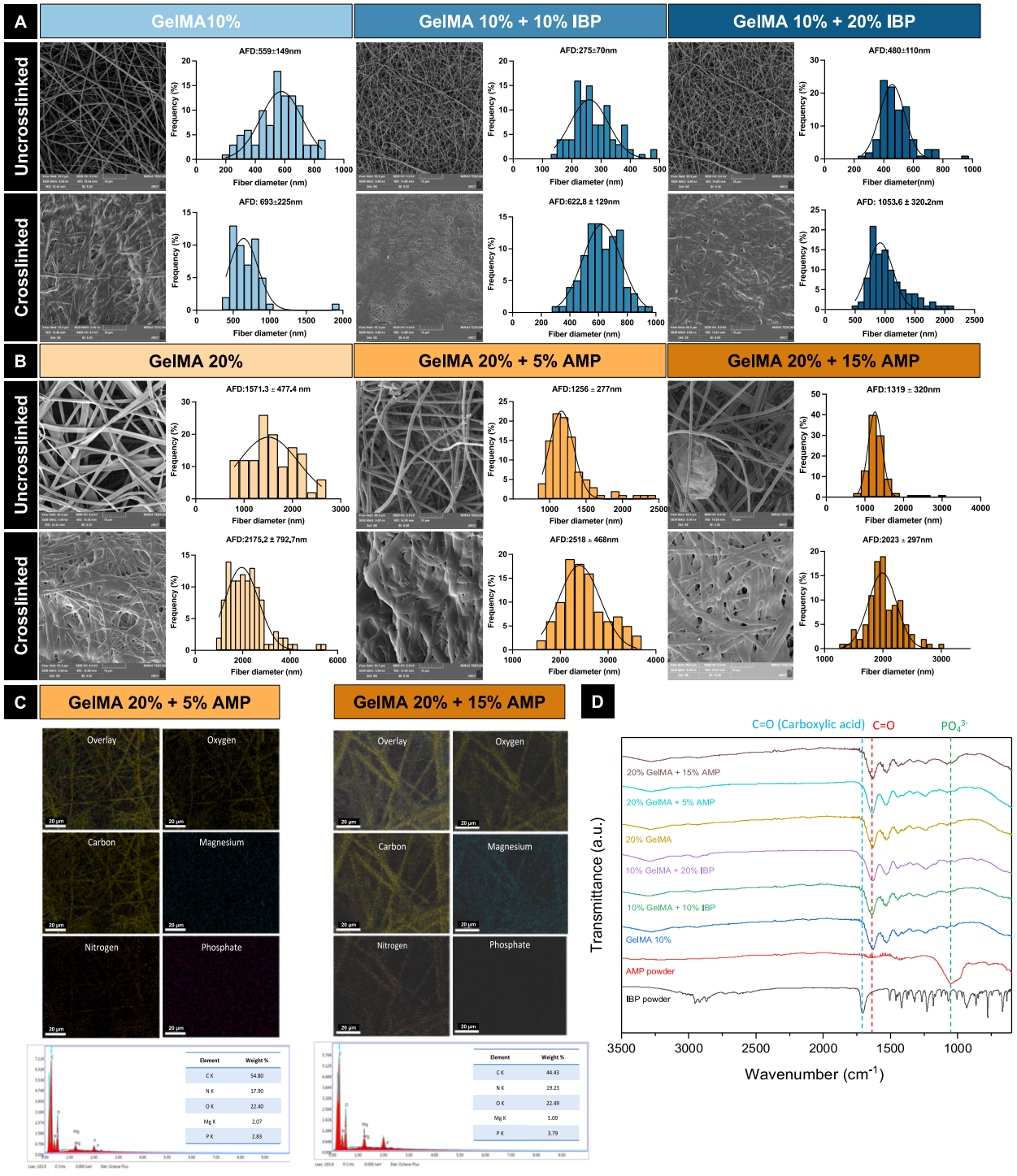

Fig. 1. Representative SEM images at 5000 × magnification of the electrospun fibers before and after cross-linking with the respective fiber diameter frequency histograms for the **(A)** Ibuprofen (IBP)-loaded fibers and **(B)** Amorphous magnesium phosphate (AMP)-incorporated fibers ($n = 150$). **(C)** Energy-dispersive spectroscopy (EDS) analysis of the fibers incorporated with AMP. **(D)** Fourier-transform infrared spectroscopy (FTIR) of GelMA-based fibers and as-received IBP and AMP powders ($n = 3$). Scale bar = 20 μm.

processed with GelMA 10 % (*w/v*) exhibited, on average, smaller fiber diameters compared to GelMA 20 % (w/v) fibers, as higher solution concentrations lead to larger fiber diameters due to increased viscosity, which reduces jet elongation during electrospinning (Fig. 1A-B) [29]. Furthermore, all electrospun formulations exhibited an increase in fiber diameter after crosslinking, a result also observed in previous studies [13,23]. This can be explained by the photocrosslinking process, which involves wetting the fibers with isopropyl alcohol before light exposure, leading to water uptake and causing the fibers to swell (Fig. 1A-B).

Electrospun GelMA incorporated with AMP displayed a customary three-dimensional porous network consisting of randomly oriented fibers. However, after crosslinking, AMP-incorporated fibers also displayed noticeable swelling, as previously explained (Fig. 1B). Importantly, EDS analysis confirmed the integration of AMP particles within the fibers, detecting the primary elements of AMP, such as magnesium (Mg), phosphorus (P), and oxygen (O) [30]. As expected,

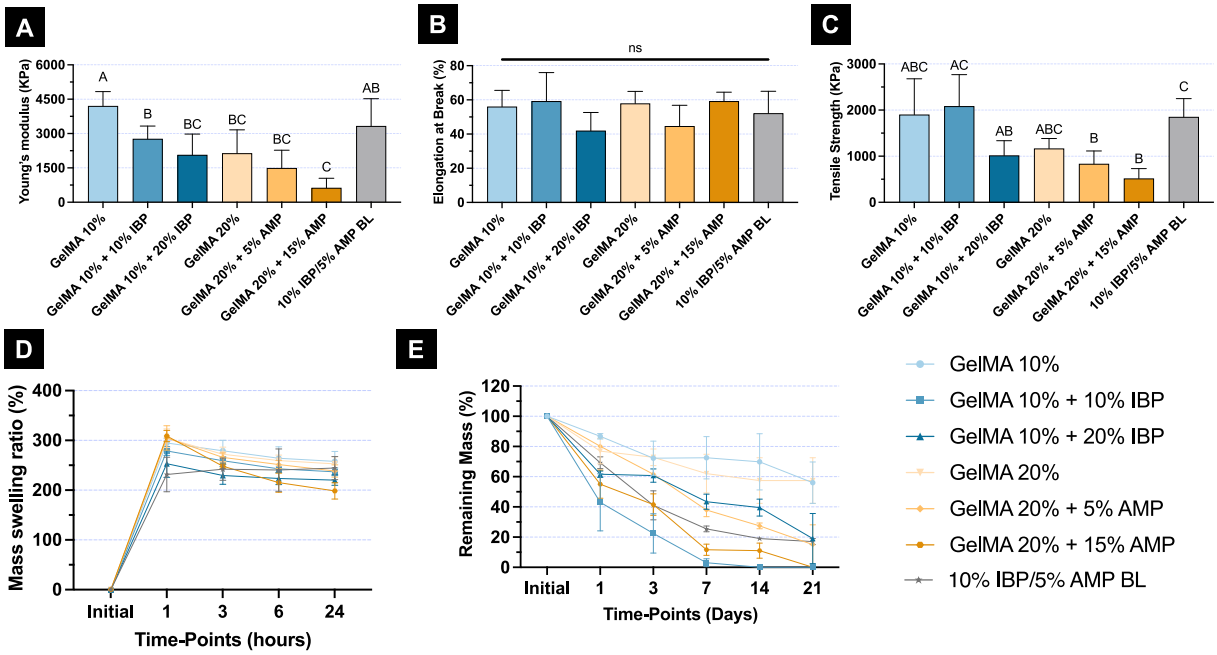

Fig. 2. Mechanical characterization of individual electrospun layers and bilayer scaffolds loaded with 10 % IBP and 5 % AMP after 1 h in PBS. **(A)** Young's modulus, **(B)** Elongation at break, and **(C)** Tensile strength. Mean and standard deviation. Different letters indicate significant statistical differences. ns = no significant difference was found. (Welch's ANOVA/Games-Howell; $n = 6$; $\alpha = 5$ %). **(D)** Swelling ratio and **(E)** degradation profile of individual layers and bilayer loaded with 10 % IBP and 5 % AMP in PBS with collagenase (1 U/mL) at 37 °C. Mean and confidence interval ($n = 6$; CI 95 %).

electrospun fibers containing 15 % AMP displayed higher mass percentages of Mg and P compared to those with 5 % AMP (Fig. 1C). The chemical composition of the electrospun fibers was analyzed by FTIR, revealing the characteristic peaks of GelMA, such as C═O stretching (amide I) and C═C stretching of the methacrylate groups (~1600 cm^{-1}) [13,23]. Pure IBP and AMP powders were also analyzed individually, showing their characteristic peaks: C═O stretching of the carbonyl group from the carboxylic acid functional group (~1700 cm^{-1}) for IBP [31,32], and PO_4^{3-} stretching of the phosphate group (~1040 cm^{-1}) for AMP [16]. These peaks were more prominent in fibers incorporating higher concentrations of these compounds (GelMA 10 % + 20 % IBP and GelMA 20 % + 15 % AMP) (Fig. 1D).

The evaluation of the electrospun fibers' mechanical properties demonstrated that the incorporation of IBP and AMP influenced the material stiffness (Young's modulus), as well as resistance to break under tension. At the same time, no significant effects were observed on their ductility (elongation at break) (Fig. 2A-C). A significant decrease in Young's modulus values was observed for all groups containing IBP, as well as for the GelMA 20 % groups, regardless of AMP incorporation, compared to the GelMA 10 % group ($p < 0.05$) (Fig. 2A). Lower tensile strength values were observed in the GelMA 10 % + 20 % IBP and GelMA 20 % groups (with or without AMP) compared to the GelMA 10 % and GelMA 10 % + 10 % IBP groups; however, no statistical differences were detected between these groups ($p > 0.05$), except for the GelMA 10 % + 10 % IBP group, which exhibited significantly ($p < 0.05$) higher tensile strength compared to the GelMA 20 % + 5 % AMP and GelMA 20 % + 15 % AMP (Fig. 2C). The bilayer scaffold exhibited a distinct mechanical performance, showing higher Young's modulus, statistically similar to the GelMA 10 % group ($p > 0.05$) (Fig. 2A), and tensile strength values comparable to both the GelMA 10 % and GelMA 10 % + 10 % IBP groups ($p > 0.05$) (Fig. 2C).

Incorporating compounds, such as IBP and AMP, into electrospun fibers can alter their mechanical properties by disrupting the polymer network, potentially affecting fiber structure through interactions between the compounds and the polymer matrix, a phenomenon also reported in previous studies [11,33]. Although the incorporation of IBP and AMP affected the mechanical properties of the electrospun layers, we found that all synthesized formulations, particularly the bilayer scaffold, exhibited stiffness values compatible with those of human dental pulp tissue, which ranges around 5.5 ± 2.8 kPa [34]. Mimicking the native pulp tissue's stiffness is crucial, as it can modulate cell behavior, such as adhesion, proliferation, and differentiation, while providing the structural support necessary for tissue regeneration in VPT strategies [35,36].

3.2. Swelling capacity and degradation behavior

All the fabricated GelMA-based fibers tend to absorb water in biological environments. To understand this critical aspect, we investigated the distinct electrospun fiber formulations' swelling capacity associated with their hydrophilic nature [11]. Hydrophilic surfaces can enhance cell adhesion to biomaterials, thereby promoting cell proliferation and differentiation, which are essential for tissue regeneration [37]. All fiber compositions exhibited similar swelling capacities, with a rapid increase observed during the first hour of assessment. The swelling ratios reached approximately 300 % for GelMA 10 %, GelMA 20 % + 5 % AMP, and GelMA 20 % + 15 % AMP groups, ~ 275 % for GelMA 10 % + 10 % IBP, ~ 250 % for GelMA 10 % + 20 % IBP, and ~ 230 % for the bilayer formulation, compared to the initial time point (0 h). After 3 h, the bilayer formulation showed a slight increase in its swelling ratio (~240 %), while the other groups exhibited a slight reduction. From 6 to 24 h, all groups demonstrated a steady profile, with swelling ratios of ~260 % for GelMA 10 % and GelMA 20 %, ~ 240 % for GelMA 10 % + 10 % IBP, GelMA 20 % + 5 % AMP, and the bilayer formulation, ~ 220 % for GelMA 10 % + 20 % IBP, and ~ 200 % for GelMA 20 % +15 % AMP (Fig. 2D). Incorporating different compounds, such as drugs or inorganic particles, into electrospun fibers can negatively affect their swelling capacity, as observed in previous studies [23,27,38]. However, our findings showed that incorporating IBP or AMP into the formulated fibrous layers did not significantly affect their swelling capacity, as all formulations demonstrated comparable swelling ratios.

We also evaluated electrospun fibers degradation, as their longevity and the time available for cell attachment and proliferation should ideally align with the rate of new tissue formation [35]. After 1 day, the

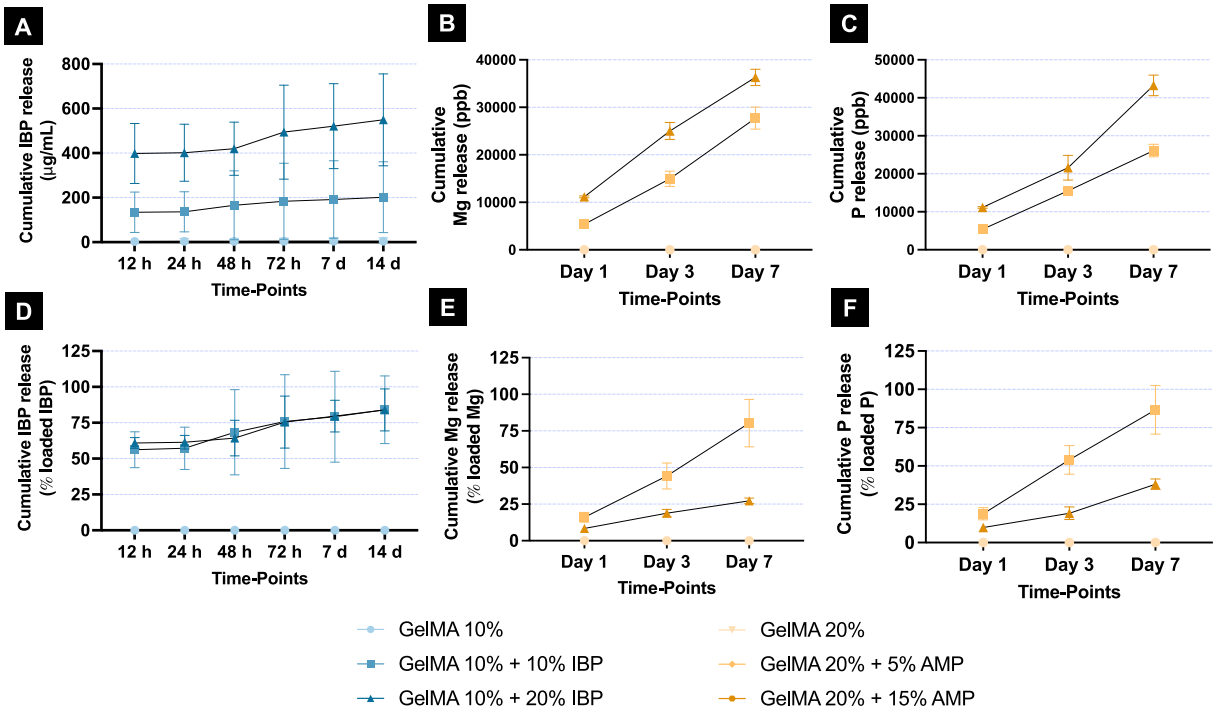

Fig. 3. **(A)** Drug release profile and **(D)** Release efficiency of individual layer loaded with IBP in PBS at 37 °C. Mean and confidence interval (n = 3; CI 95 %). **(B/C)** Ion release profile and **(E/F)** Release efficiency of individual layer incorporated with AMP in ultrapure water at 37 °C. Mean and confidence interval ($n = 4$; CI 95 %).

highest degradation was observed for the GelMA10 % + 10 % IBP group, with a mass loss of ~60 %. In contrast, lower mass losses were detected for GelMA 10 % (~12 %), GelMA 10 % + 20 % IBP (~40 %), GelMA 20 % (~22 %), GelMA 20 % + 5 % AMP (~20 %), GelMA 20 % + 15 % AMP (~45 %), and the bilayer formulation (~30 %). This pattern continued until day 21, except for the GelMA 10 % + 10 % IBP group, which was almost completely degraded by day 7. At day 21, the remaining mass was ~42 % for both 10 % and 20 % GelMA, ~82 % for GelMA 10 % + 20 % IBP, ~83 % for GelMA 20 % + 5 % AMP, and ~ 82 % for the bilayer formulation. In comparison, the GelMA 20 % + 15 % AMP group underwent complete degradation (Fig. 2E). This degradation profile corresponds closely to the timeline of dentin-like tissue formation by progenitor cells, as previously demonstrated, where pulp capping with calcium hydroxide led to the formation of a tubular dentin-like matrix lined with odontoblast-like cells after 28 days [39].

3.3. Release kinetics (IBP and AMP)

The release of drugs or therapeutic ions from biomaterials can directly influence their bioactivity by modulating molecular and cellular behaviors such as signaling pathway activation, inflammatory responses, proliferation, and differentiation [35]. Since our electrospun fibers were incorporated with IBP and AMP, assessing the release of IBP as well as magnesium and phosphate ions over time is crucial to determine their bioactive potential. As expected, fibers containing 20 % IBP released higher drug concentrations than those with 10 %, yet both formulations ensured a sustained IBP release over 14 days (Fig. 3A). Regardless of the initial IBP loading in GelMA, both IBP-loaded groups exhibited a similar release efficiency, with each releasing more than 80 % of the incorporated drug within 14 days (Fig. 3D). This consistent release underscores their potential to reduce the local inflammatory response, promote quick resolution of inflammation, and improve the regenerative process [40].

Additionally, fibers with AMP showed a gradual release of magnesium (Mg) and phosphate (P) ions over time, with higher concentrations observed in fibers containing 15 % AMP compared to those with 5 % (Fig. 3B-C). Although the 5 % AMP formulation released almost the entire incorporated content (>80 %), the 15 % formulation liberated a lower proportion of its theoretical load (Fig. 3E-F). This behavior is consistent with the typical non-linear release observed in hydrogels containing increasing amounts of inorganic fillers. Higher AMP loading tends to promote particle aggregation, reduce effective surface area, and form a denser GelMA network, limiting medium penetration and solute diffusion [41,42]. Additionally, local accumulation of Mg and P around AMP clusters may create a self-limiting microenvironment that prevents further dissolution. This ongoing ion release can provide essential signals for cell differentiation and mineralization, potentially enhancing dentin-like tissue formation by progenitor cells [18,35].

3.4. DPSC spreading, adhesion, and viability on the electrospun fibrous layers

The ability of DPSCs to adhere, spread, and proliferate on biomaterials is a critical factor for successful dentin-like tissue regeneration. With fluorescence microscopy, we observed well-spread cells in the GelMA-based electrospun fiber formulations, with actin filament staining indicating an organized cytoskeletal structure, suggesting firm cell attachment (Fig. 4A). The affinity of DPSCs to GelMA is well-documented, making it an excellent scaffold for regenerative dentistry [13,43–48]. This can be attributed to its biomimetic extracellular matrix-like composition, cell-adhesive features (*e.g.*, Arg-Gly-Asp sequences), swelling, and mechanical properties that support cell attachment, nutrition, and proliferation [44,48]. SEM analysis further confirmed these findings, as cells exhibited extended filopodia actively interacting with the fibrous networks (Fig. 4B). These interactions are essential for cellular communication, migration, and differentiation, which are key processes in dentin-pulp regeneration [49,50]. Incorporating IBP or AMP did not negatively impact these features. However, it is possible to notice that the higher incorporated concentrations (*i.e.*, 20 % IBP and 15 % AMP) presented fewer cytoplasmic extensions during the first 3 days. This indicates an influence of the molecules on the early cell-substrate interactions, possibly due to alterations in surface

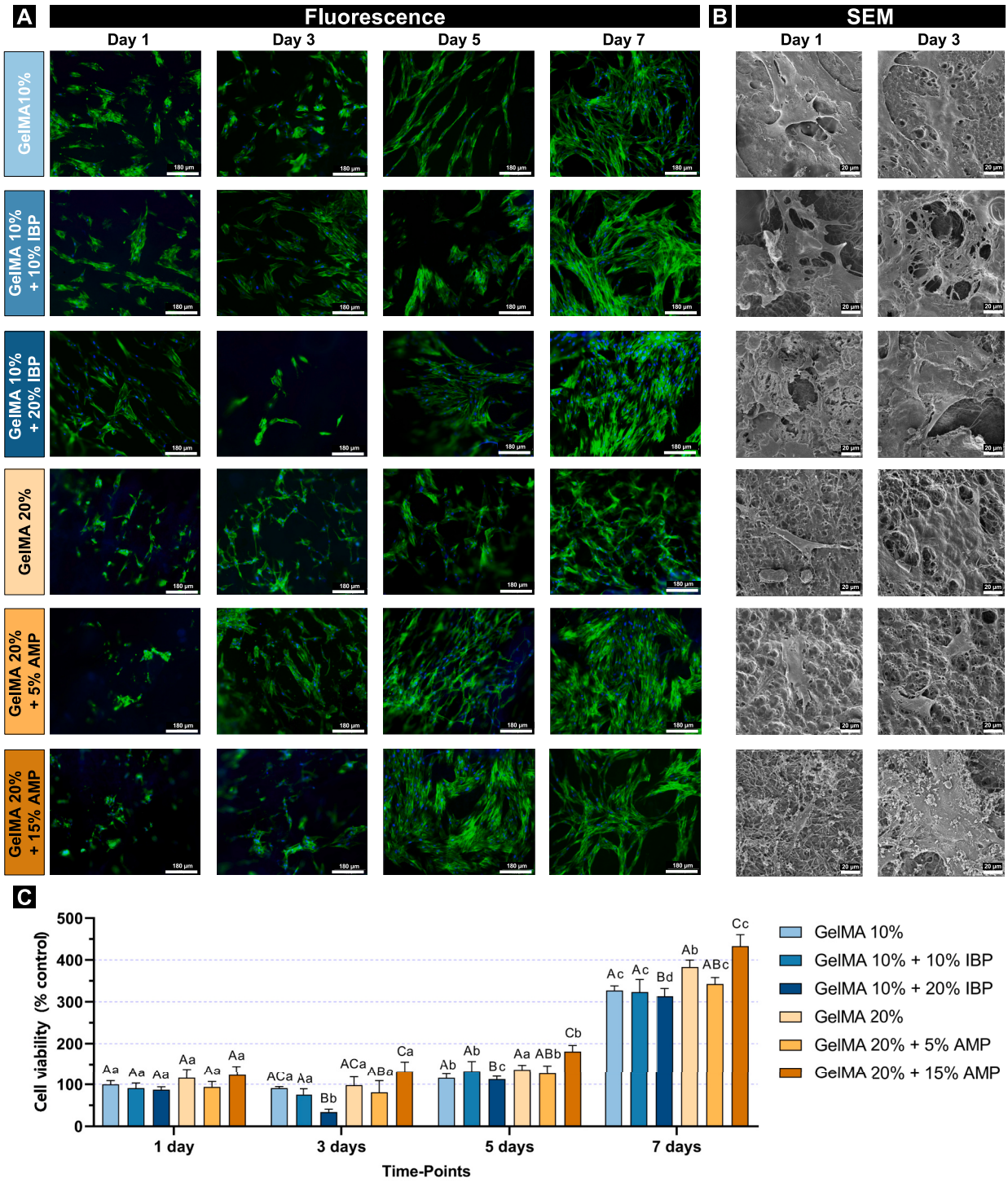

Fig. 4. **(A)** Dental pulp stem cells (DPSC) adhesion and spreading on the surface of the electrospun fibers (10× magnification). Actin filaments (Green) were stained with ActinGreen 488 reagent, and cell nuclei (blue) were labeled with DAPI. Scale bar = 180 μm. **(B)** DPSC morphology on the fibers' surface (SEM images 2000 × magnification). Scale bar = 20 μm. **(C)** Viability of DPSC seeded on the surface of the electrospun fibers. Mean and standard deviation. Different capital letters indicate significant differences between groups within each time-point. Different lowercase letters demonstrate significant differences between time-points within each group (repeated measures ANOVA/Sidak's post-hoc; $n = 6$; $\alpha = 5$ %). (For interpretation of the references to colour in this figure legend, the reader is referred to the web version of this article.)

chemistry and ionic changes that could lead to transient effects on cell adhesion signaling pathways. The higher IBP concentration may have modulated integrin-mediated attachment by interfering with prostaglandin signaling, which can either promote or inhibit integrin expression and function through different signaling pathways [51,52]. On the other hand, the high solubility of AMP could have led to localized ionic modulation, increasing Mg^{2+} availability and temporarily affecting the migration, organization, spreading, and differentiation of mesenchymal stem cells [53–55].

All electrospun fiber compositions increased DPSC metabolism over

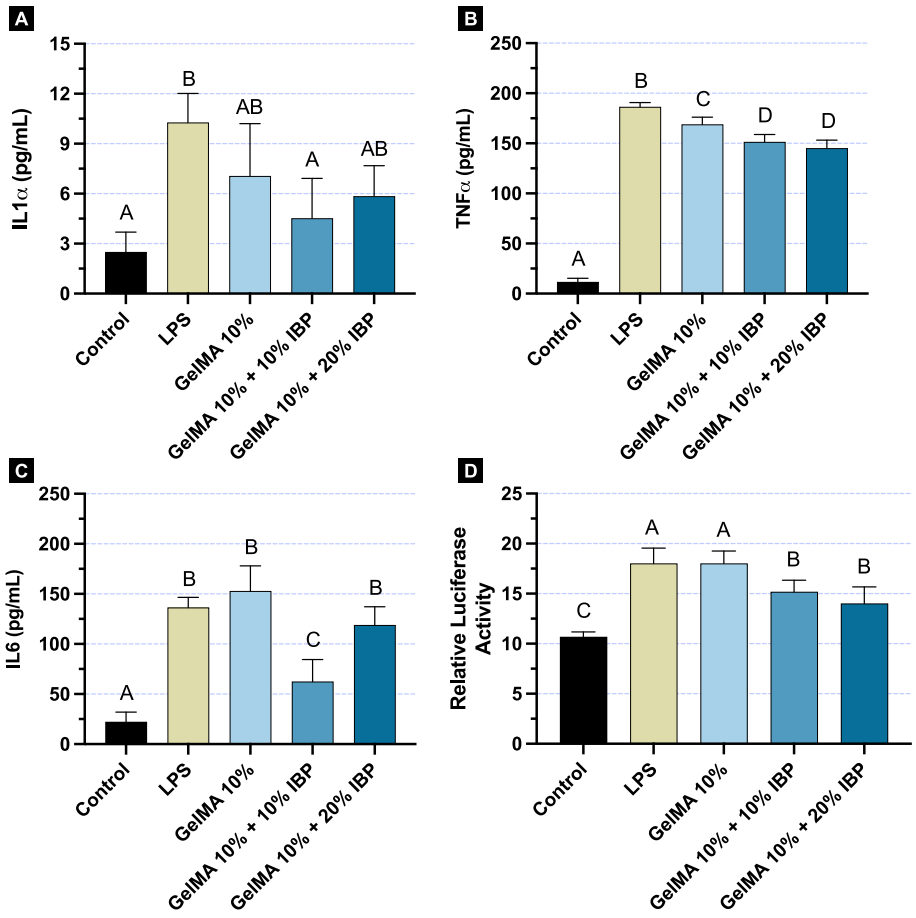

Fig. 5. (A–C) Synthesis of pro-inflammatory cytokines by macrophages (RAW 264.7) stimulated with 0.1 μg/mL of lipopolysaccharides from *E. coli* for 24 h. Mean and standard deviation (ANOVA/Tukey's; n = 4; α = 5 %). **(D)** NF-ĸB luciferase activity exposed to scaffold extracts *via* transwell. Mean and standard deviation. (ANOVA/Tukey's; n = 6; α = 5 %). Different letters indicate significant statistical differences. ns = no significant difference was found.

time (Fig. 4C). This confirms that the GelMA-based formulations provided a cytocompatible microenvironment, allowing cells to proliferate. Interestingly, the presence of AMP increased cell metabolism compared to the control group (pure GelMA fibers). The controlled release of Mg^{2+} may have modulated cell processes related to proliferation, including cell cycle regulation, protein synthesis, and intracellular signaling pathways [56–58]. Therefore, considering that pulp regeneration requires active stem cell proliferation before differentiation, AMP incorporation could offer a clinical benefit by accelerating the early stages of tissue repair [59,60].

On the other hand, IBP incorporation reduced DPSC viability after 3 days (Fig. 4C). However, after 7 days, cells cultured on the IBP-laden fibers recovered metabolic activity compared to the control. We attribute this effect to the dose-dependent action of NSAIDs on stem cell behavior, as they modulate signaling pathways involved in apoptosis, cell proliferation, differentiation, and extracellular matrix remodeling [21,61,62]. Achieving a balance between inflammation and tissue regeneration was a critical factor in scaffold design, especially given that excessive suppression of inflammation could compromise the reparative potential of progenitor cells [8,63]. Considering this, the burst release of IBP may have influenced cell viability during the first few days, but this was not detrimental over time, allowing for proper cell proliferation, especially in the case of the GelMA 10 % + 10 % IBP formulation.

3.5. Anti-inflammatory effects of IBP-loaded electrospun layer on macrophages

The IBP-laden layer was designed to regulate the immune response, acknowledging the two-edged role of inflammation in pulp regeneration. While acute inflammation is imperative for initiating tissue repair, its persistence can lead to irreversible damage and necrosis [63]. In this study, IBP-laden fibers markedly lowered IL-1α, TNF-α, and IL-6 production in LPS-activated macrophages (Fig. 5A-C). Clinically, these are among the initial cytokines released following microbial invasion. They first recruit immune cells, but their prolonged overexpression leads to tissue degradation, pain, and ultimately impairs healing in chronic pulpitis [64,65].

The decline in NF-κB activity seen in the macrophage cultures exposed to IBP-laden fibers (Fig. 5D) emphasizes the anti-inflammatory effect of the GelMA-based fibers containing IBP. NF-κB is a master switch in the bacterial-triggered inflammatory cascade: when cell receptors detect endotoxins, such as LPS, NF-κB moves to the nucleus and triggers the transcription of a wide array of pro-inflammatory cytokines [25,66]. Although IBP is best known for inhibiting cyclooxygenase (COX) enzymes, this COX blockade can also indirectly control NF-κB signaling. Consequently, the sustained release of IBP from the fibers not only diminishes macrophage activation but also limits downstream NF-κB-mediated cytokine production, thereby broadening its overall anti-inflammatory effect [67,68].

It is essential to note that in our experiments, IBP did not completely block NF-κB activity. This may be beneficial, given the previously discussed role of inflammation in recruiting progenitor cells and initiating tissue repair [8,63]. The fibers containing higher IBP concentration showed a less pronounced reduction in IL-6 synthesis. IL-6 plays pro-inflammatory and regenerative roles in tissue regeneration, including involvement in ECM remodeling, progenitor cell recruitment, and

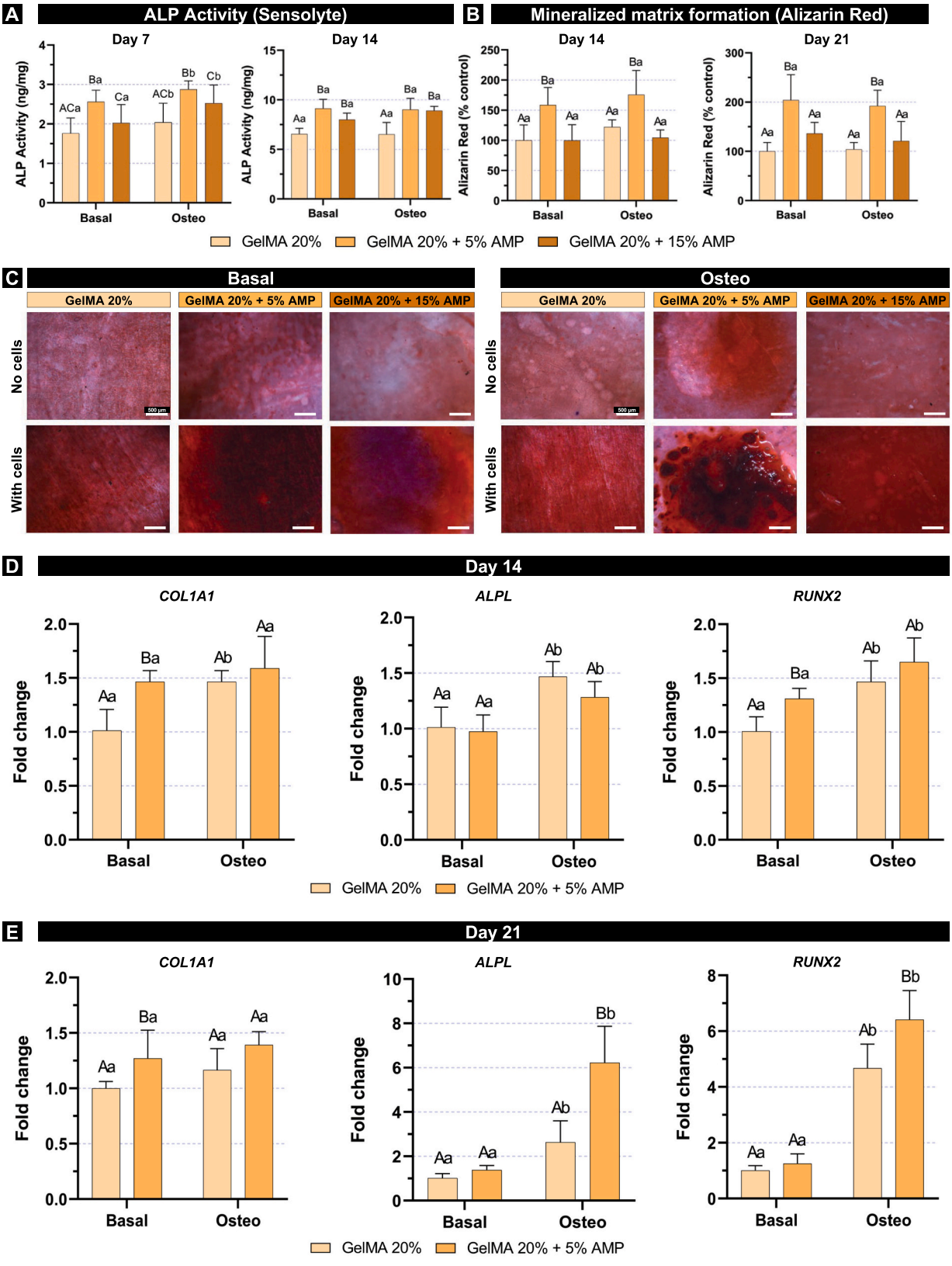

Fig. 6. **(A)** ALP activity, **(B)** Mineralized matrix formation, and **(D)** Gene expression of DPSC seeded on the distinct fibers' surface. Mean and standard deviation. Different capital letters indicate significant differences between groups within each media condition. Different lowercase letters demonstrate significant differences between media conditions within each group (ANOVA/Tukey's or Games-Howell's *post hoc*; $n = 6$; $\alpha = 5$ %). **(C)** Representative images of fibers' surface (1.25 × magnification) after 21 days of culture (Alizarin red staining). Scale bar = 500 μm. (For interpretation of the references to colour in this figure legend, the reader is referred to the web version of this article.)

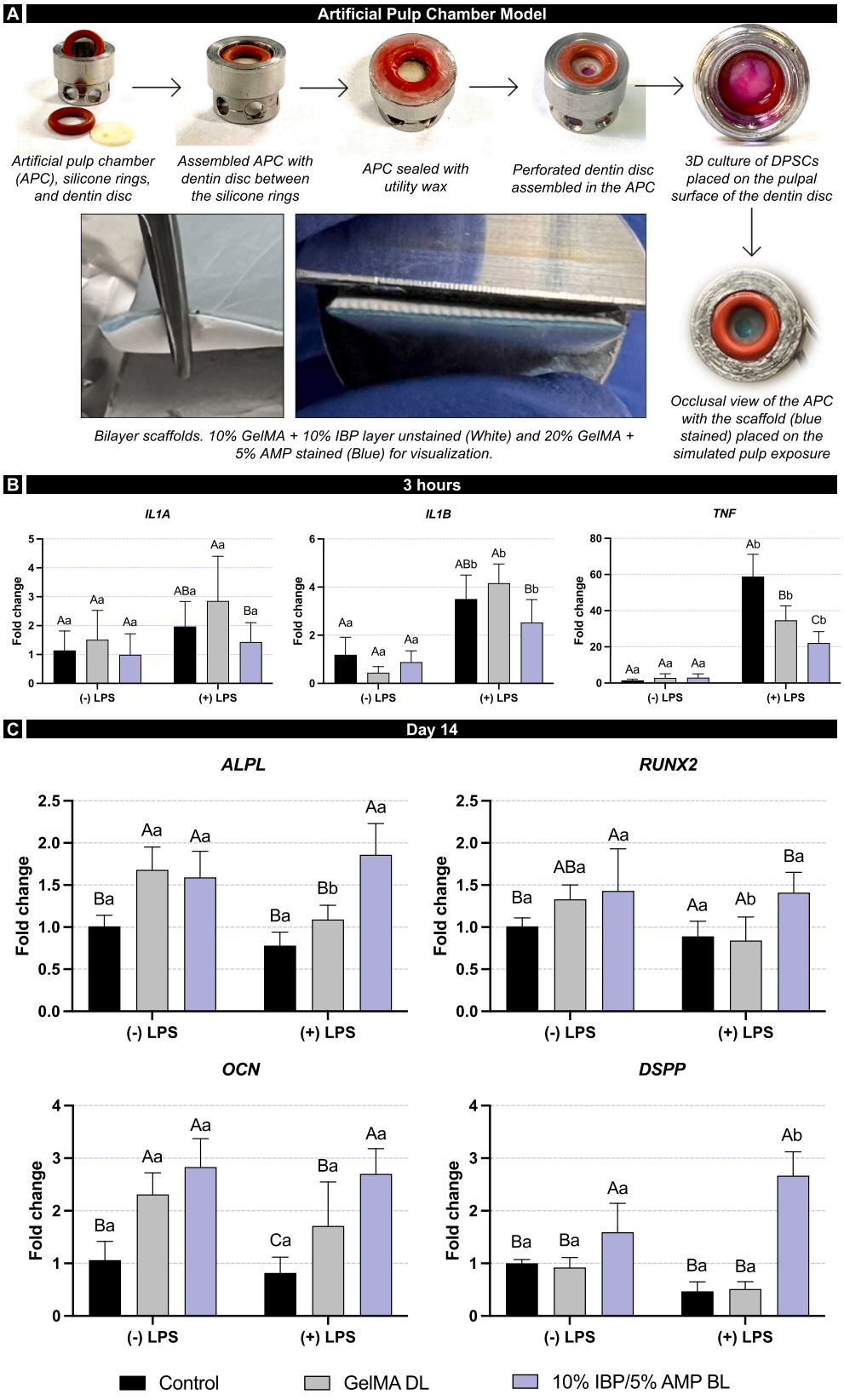

Fig. 7. **(A)** Schematic representation of the APC model and gene expression of DPSC in the APC model with or without LPS stimulus after **(A)** 3 h and **(B)** 14 days in contact with the bilayer scaffolds. Mean and standard deviation. Different capital letters indicate significant differences between groups within each media condition. Different lowercase letters demonstrate significant differences between media conditions within each group (Two-way ANOVA/Sidak's *post hoc*; n = 6; α = 5 %).

differentiation [64,69,70]. From a clinical perspective, these findings suggest that IBP-laden fibers could be a promising treatment strategy for managing pulpitis, where controlling inflammation is crucial for preserving pulp vitality.

Current VPT materials, such as calcium hydroxide and calcium silicate-based cements, stimulate reparative responses through dystrophic calcification but lack active control over inflammation [71–73]. Thus, an IBP-releasing scaffold could provide an immediate anti-inflammatory effect while maintaining a microenvironment conducive to regeneration. Supporting this, we found the IBP release profile exhibited a sustained pattern, with an initial burst release in the first few hours, followed by a gradual release over several days. This suggests that the scaffold can provide immediate anti-inflammatory action during the acute phase of pulp inflammation, while its sustained release may help prevent secondary inflammatory events. The controlled release also presents an advantage over oral NSAIDs, which require repeated dosing and are associated with systemic side effects [74].

3.6. Odontogenic effects of AMP-incorporated electrospun layer on DPCSs

To evaluate the odontogenic potential of the AMP-incorporated layer, we evaluated ALP activity, mineralized matrix formation, and gene expression of osteogenic markers over time. Alkaline phosphatase (ALP) activity was quantified at 7 and 14 days (Fig. 6A). At 7 days, ALP activity was significantly higher in the 5 % AMP group compared to pure GelMA under both basal and osteogenic conditions ($p \leq 0.005$). By day 14, all AMP-incorporated groups presented higher ALP activity than the control group. The increased ALP activity in AMP-containing fibers, notably in the 5 % AMP group, highlights the intrinsic bioactivity of AMP in promoting early odontogenic differentiation. Our findings suggest that AMP actively modulates cell behavior through ionic dissolution products (*e.g.*, Mg^{2+} and PO_4^{3-}), which are known to stimulate osteo/odontogenic pathways [18,30]. This is consistent with prior studies demonstrating AMP's capacity to enhance osteogenic gene expression and mineral deposition without the need for external growth factors [18]. The responsiveness under both basal and osteogenic conditions shows AMP's potential to act as a molecular signaling agent in the proposed bilayer scaffold.

To assess the dentin regeneration potential, mineralized matrix formation was evaluated *via* Alizarin Red staining at 14 and 21 days (Fig. 6B). The 5 % AMP group under both basal and osteogenic conditions demonstrated the highest mineral deposition at day 14 ($p \leq 0.002$), which remained significantly elevated at day 21 ($p < 0.0001$), as corroborated by exemplary staining images (Fig. 6C). Quantitative analysis revealed that AMP-incorporated layer markedly outperformed the control (pure GelMA fibers), supporting AMP's pro-mineralizing effect. This increased mineralization can be attributed to the amorphous nature of the magnesium phosphate. Unlike crystalline magnesium phosphate, which has limited resorption and bioavailability, amorphous magnesium phosphate (AMP) offers enhanced ion release kinetics, promoting cell-mediated biomineralization processes [30,75]. AMP's rapid yet controlled dissolution leads to a sustained release of ions, resulting in more extensive calcium phosphate deposition, improved cellular adhesion, and higher mineralization rates compared to conventional magnesium phosphate ceramics [75]. Altogether, these findings highlight AMP's intrinsic bioactivity, making it a promising candidate for regenerating the dentin-pulp complex and other mineralized tissues.

Gene expression analyses at 14 and 21 days further supported the odontogenic potential of AMP-containing fibers by demonstrating upregulation of key osteogenic markers, including *COL1A1*, *ALPL*, and *RUNX2* (Fig. 6D-E). Under basal conditions at day 14, the AMP groups exhibited increased *COL1A1* and *RUNX2* expression ($p \leq 0.0011$), suggesting an early induction of the osteo/odontogenic phenotype. By day 21, this effect was amplified under osteogenic conditions, with *RUNX2* levels upregulated approximately 6-fold relative to baseline ($p = 0.0007$). Although *COL1A1* expression was also upregulated, its increase was more modest, aligning with its role in early matrix formation rather than late-stage mineralization [76]. The sustained upregulation of *RUNX2*, a master gene for osteogenic differentiation, and *ALPL*, which drives matrix maturation and mineralization, indicates that AMP initiates and then maintains odontogenic signaling toward dentin formation, corroborating earlier findings of its bioactivity in dental pulp stem cells [18].

The presence of inflammation in the pulp tissue can impair the formation of mineralized matrix, leading to less effective outcomes in pulp exposure repair and sealing. Based on the previous experiments, 10 % IBP and 5 % AMP were selected for bilayer scaffold fabrication. We evaluated our bilayer scaffold using an artificial pulp chamber model with a 3D culture of DPSCs to simulate the release profile and its therapeutic effects in contact with exposed tissue, first modulating inflammation (IBP layer) and then inducing mineralized matrix formation (AMP layer). Gene expression analysis at 3 h revealed that LPS stimulation significantly upregulated pro-inflammatory cytokines *IL1A*, *IL1B*, and *TNF* in all groups (Fig. 7B). Among LPS-treated samples, the bilayer scaffold containing 10 % IBP and 5 % AMP downregulated *IL1A*, *IL1B*, and *TNF* expression compared to the control (non-treated DPSC's 3D cultures) and GelMA bilayer ($p \leq 0.0488$). This result was expected based on the anti-inflammatory role of IBP, as discussed earlier. The downregulation of *TNF* observed in the GelMA group compared to the untreated LPS-stimulated 3D culture was likely due to the immunomodulatory properties of the GelMA matrix. GelMA hydrogels can sequester soluble TNF-α, reducing its bioavailability and consequently disrupting the positive feedback loop necessary for sustained TNF gene expression [77]. This suggests that, in addition to the action of IBP, the scaffold's base material may contribute to the attenuation of inflammation, creating a more favorable environment for subsequent tissue repair.

After 14 days of 3D culture, the expression of odontogenic and osteogenic markers (*ALPL*, *RUNX2*, *OCN*, and *DSPP*) was significantly upregulated in groups treated with the bilayer scaffold containing 10 % IBP and 5 % AMP compared to the non-treated DPSC's 3D cultures (control) (Fig. 7C). Among all conditions, the bilayer scaffolds exhibited the highest expression levels across all markers, with statistically significant increases in *ALPL*, *OCN*, and *DSPP* transcripts under both unstimulated and LPS-stimulated environments ($p \leq 0.0088$). Notably, *DSPP*, a key marker of odontoblast differentiation [78], was most elevated in the IBP and AMP-loaded group under inflammatory conditions, suggesting that the bilayer-loaded scaffold maintains its odontogenic potential even in a pro-inflammatory microenvironment. This response highlights the synergistic effect of the bilayer scaffold's components: the initial inflammatory modulation mediated by IBP appears to create a favorable immunological niche, which, when combined with AMP's strong capacity for mineralization induction, enhances the odontogenic differentiation cascade. Although the APC-3D culture stimulated with LPS *in vitro* model represents an improvement in the complexity of the DPSCs' response [24], it cannot fully replicate the complexity of the *in vivo* dentin-pulp interface or the dynamic immune and mechanical environment of the oral cavity. A multifunctional scaffold like the one presented here could shift the paradigm from using passive filling materials to using biologically active platforms that support tissue regeneration, even in challenging clinical scenarios.

3.7. In vivo subcutaneous response to scaffold application

The rat subcutaneous implantation model is a straightforward and cost-effective method for evaluating a scaffold's biocompatibility and immune response before it is tested at its target site or evaluated preclinically. Because implants can be retrieved easily, this test has become the standard initial screening method for new biomaterials [11,26,79].

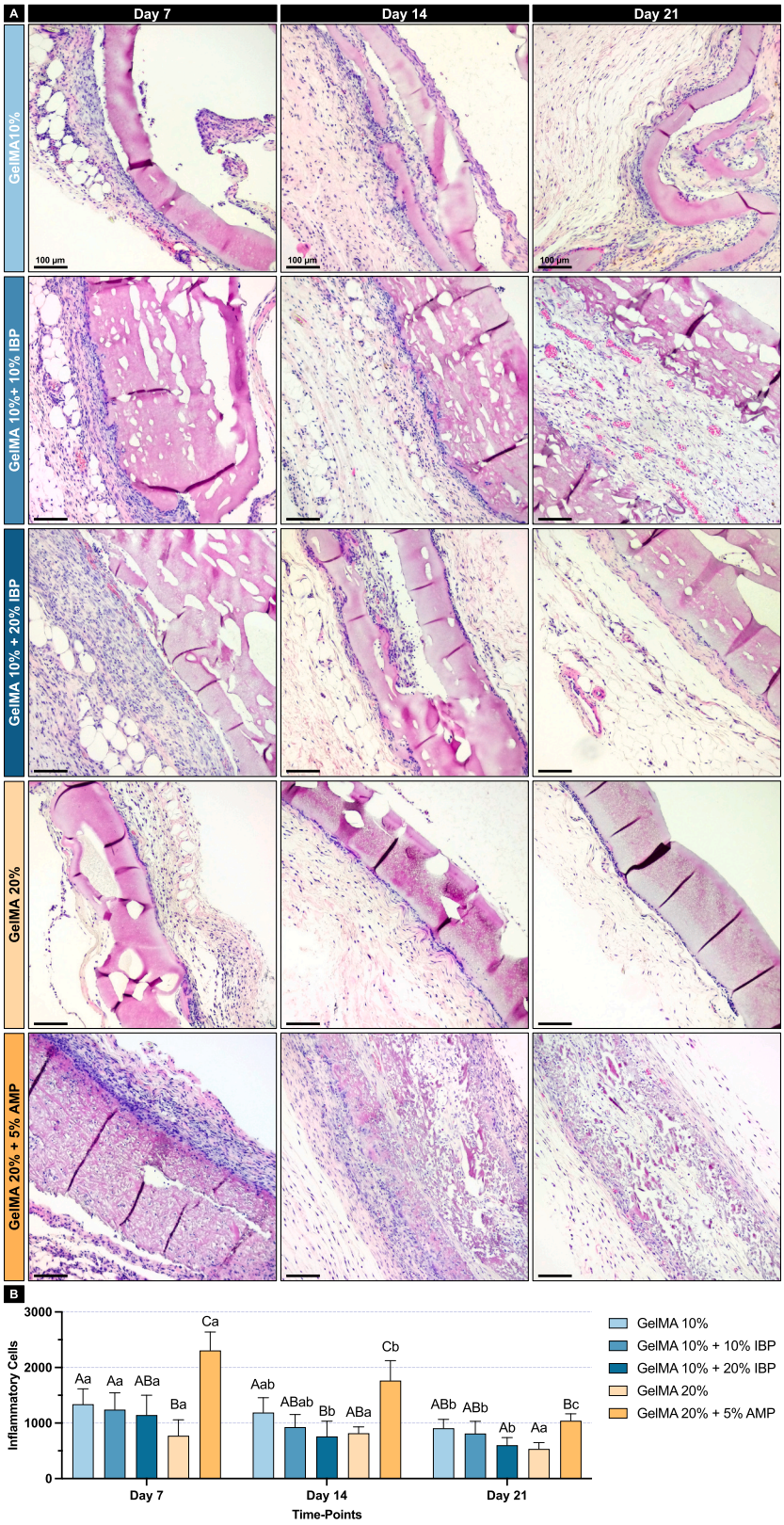

Fig. 8. **(A)** Representative images of hematoxylin and eosin (H&E) staining for each fibrous layer at 7- and 21-day post-implantation. Magnified at 100×. Scale bar = 100 µm. **(B)** Inflammatory cell count values expressed as mean ± standard deviation after ImageJ analysis. Different capital letters indicate significant differences between groups at each time point. Different lowercase letters demonstrate significant differences between time-points within each group. (Two-way ANOVA/Sidak's *post hoc*; n = 6; α = 5 %).

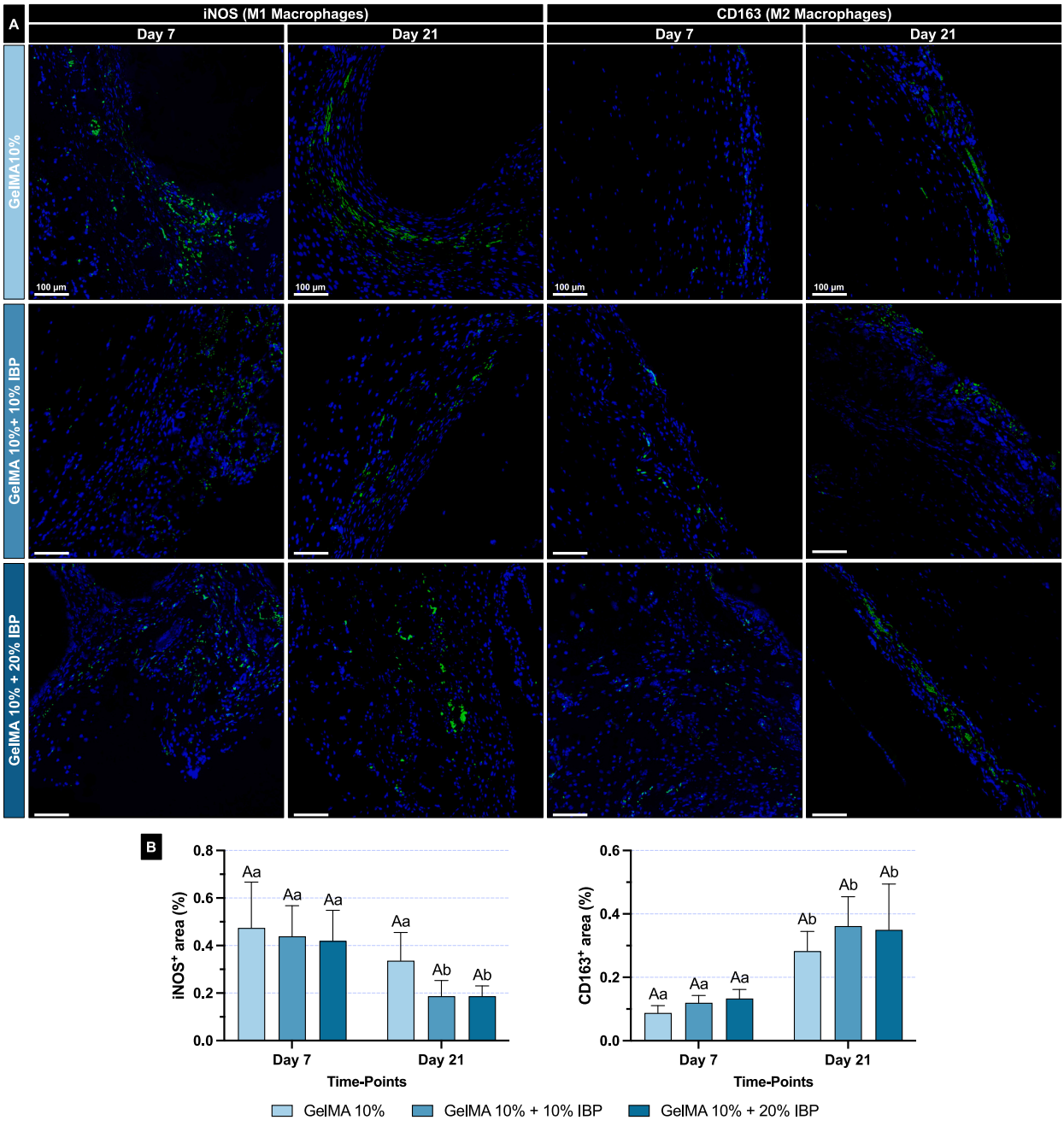

Fig. 9. *In vivo* immunolabeling of macrophage polarization markers evoked by the pure GelMA 10 % and IBP-loaded layers, **(A)** iNOS for M1 and **(B)** CD163 for M2, using secondary antibody Alexa Fluor 488 (green) at 7- and 21-days post-implantation (100× magnification). Scale bar = 100 µm. Positive immunolabeling expression area expressed as mean ± standard deviation after ImageJ analysis. Different capital letters indicate significant differences between groups at each time point. Different lowercase letters demonstrate significant differences between time-points within each group. (Two-way ANOVA/Sidak *post hoc*; n = 6; α = 5 %). (For interpretation of the references to colour in this figure legend, the reader is referred to the web version of this article.)

Here, we implanted the two layers of our bilayer scaffold separately to determine whether either one, AMP for mineralization or IBP for inflammation control, provoked an excessive foreign-body reaction. Fig. 8 combines histology, which shows how inflammatory cells accumulate around each one of the scaffold layers over time, with a graph that records the number of those cells for every group at each time point. One week after implantation, every electrospun GelMA-based fibrous sample triggered an acute inflammatory reaction, as evidenced by the numerous small, dark nuclei, representing neutrophils, macrophages, and other leukocytes surrounding the materials (Fig. 8A). The intensity, however, depended on the layer's composition. All GelMA 10 % electrospun samples, with or without IBP, attracted similar numbers of inflammatory cells. Increasing GelMA to 20 % reduced the response, but adding 5 % AMP negated that benefit, resulting in the highest inflammatory cell count at day 7 (Fig. 8B). By two weeks, inflammation had faded around all scaffolds, and early fibrous capsule tissue had started to form. The reduction in inflammatory profile was higher in the IBP-loaded samples (GelMA 10 % + 20 % IBP), indicating that the IBP dose effectively reduced the response as healing progressed. The AMP-laden GelMA 20 % layer, despite its severe reaction at day 7, also showed a markedly lower cell count at day 14, indicating that the initial spike was transient and not prolonged by the presence of AMP.

By three weeks, inflammation had essentially cleared in every group: only a few immune cells remained, and fibrous tissue was maturing

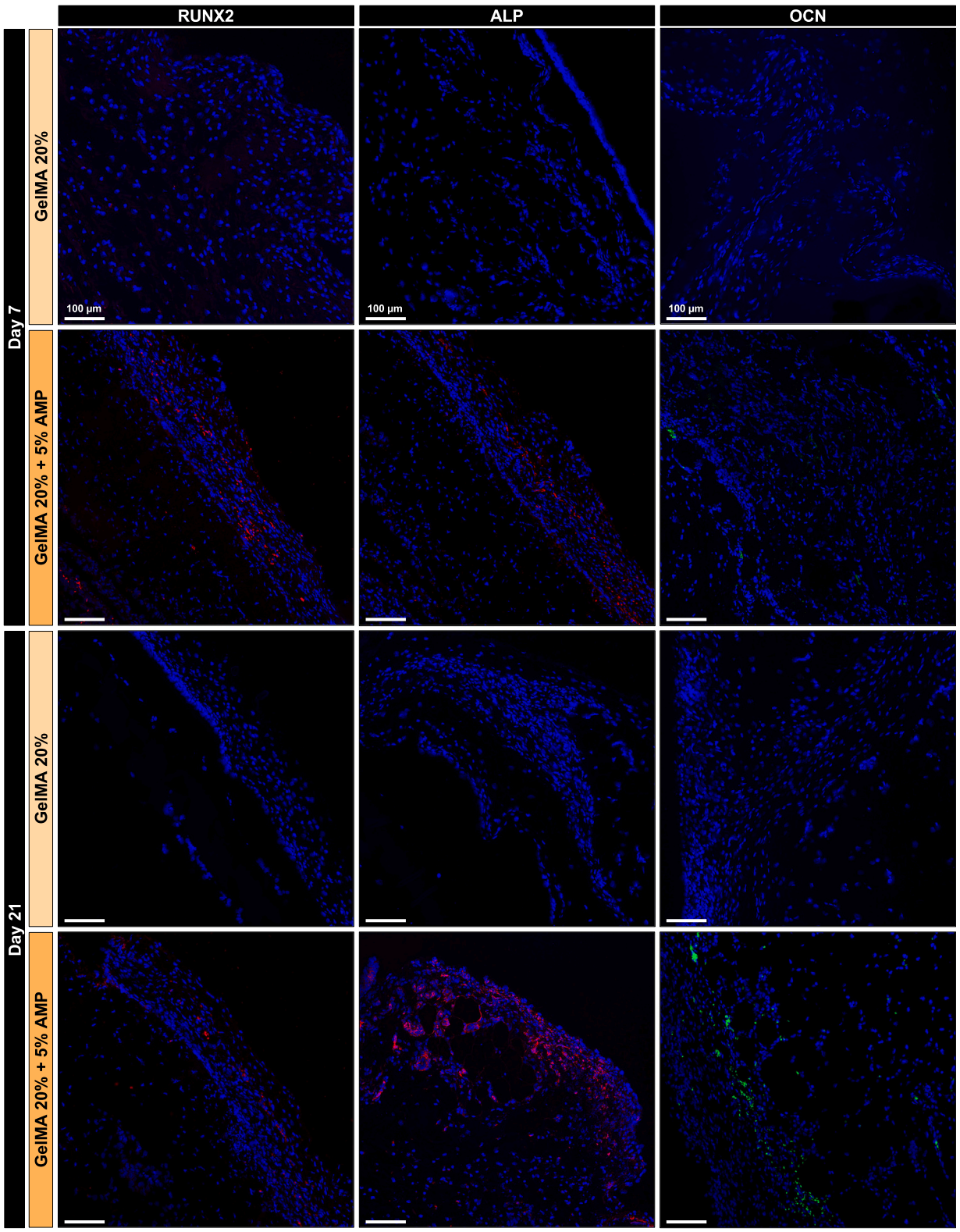

Fig. 10. *In vivo* immunolabeling of osteogenic markers by the pure GelMA 20 % and AMP-laden layer, RUNX2 and ALP using secondary antibody Alexa Fluor 594 (red), and OCN using secondary antibody Alexa Fluor 488 (green) at 7- and 21-days post-implantation (100× magnification). Scale bar = 100 µm. (For interpretation of the references to colour in this figure legend, the reader is referred to the web version of this article.)

around the scaffolds, solid evidence of biocompatibility. Inflammatory-cell counts no longer differed from those of the GelMA 10 % control. The AMP-laden layer (GelMA 20 % + 5 % AMP) reduced to the same low baseline as the GelMA 10 % and GelMA 10 % + 10 % IBP layers. The initial increase in leukocytes likely resulted from faster biodegradation, as histology indicates cell infiltration into the matrix by day 7, with most of the sample disappearing by days 14 and 21. Conversely, the pure GelMA 20 % layer, being denser and more resistant to degradation, was more difficult for cells to penetrate, resulting in a gentler initial response. Overall, each electrospun sample exhibited a pronounced drop

in inflammatory cell counts from day 7 to day 21, indicating normal healing, with histology confirming the absence of chronic inflammation in any sample, and highlighting the biocompatibility of every layer.

To determine whether IBP alters macrophage polarization, we immunolabeled sections for iNOS (a marker of M1 macrophages) and CD163 (a marker of M2 macrophages) (Fig. 9A). At day 7, the M1-positive area did not differ among the three groups ($p > 0.05$). By day 21, the GelMA 10 % control still showed the same M1 level as at day 7, whereas both IBP-loaded layers exhibited a significant decrease in M1 cells compared to their own day 7 values ($p < 0.05$) (Fig. 9B). M2 expression was low in every group at day 7, with no significant differences. By day 21, all groups showed a marked increase in CD163-positive expression ($p < 0.05$ *vs.* their respective day 7 values), and IBP did not noticeably amplify this M2 shift (Fig. 9B). Ibuprofen diminishes M1 macrophage activation by inhibiting key pro-inflammatory pathways. As an NSAID anti-inflammatory drug, IBP blocks cyclooxygenase (COX-1 and COX-2), reducing prostaglandin levels and inhibiting upstream inflammatory signals. This leads to decreased activation of the NF-κB and JAK/STAT pathways in macrophages, thereby restricting the expression of M1-associated cytokines, such as TNF-α and IL-6, as we previously observed for this layer *in vitro* [80,81]. This shift from M1 to M2 promotes a regenerative environment, as M2 macrophages release anti-inflammatory cytokines, such as IL-10 and TGF-β, along with growth factors that support angiogenesis and tissue repair. Therefore, in contexts like VPT, reducing the M1 inflammatory state to lower its ratio relative to the anti-inflammatory M2 phenotype is crucial for optimal tissue healing [8,82,83].

To determine if the AMP-containing scaffold layer triggered an osteogenic response *in vivo*, sections were immunolabeled for RUNX2, ALP, and OCN (Fig. 10). RUNX2 is a key regulator indicating early osteoblast differentiation, ALP is an enzyme that supports extracellular matrix mineralization, and OCN is a bone matrix protein produced by mature osteoblasts. Since subcutaneous tissue is a non-bone (ectopic) site, overall osteogenic activity was expected to be low. Therefore, we assessed these markers qualitatively by noting the presence or absence of staining rather than measuring them quantitatively. At both 7- and 21-day post-implantation, GelMA 20 % (without AMP) showed no detectable RUNX2, ALP, or OCN staining, as expected for a material lacking osteoinductive components. In contrast, the GelMA 20 % + 5 % AMP layer induced an osteogenic marker response with a clear temporal pattern. At 7 days, the AMP-containing group showed positive RUNX2 staining (indicating early osteogenic differentiation), whereas ALP and OCN were largely absent at this early time point. By 21 days, RUNX2 staining in the AMP group had diminished to near-baseline levels, but both ALP and OCN staining became much more pronounced. This inverse pattern is consistent with the roles these markers play in osteogenesis. RUNX2 is typically upregulated during the initial commitment of progenitors and then downregulated as osteoblasts mature. At the same time, ALP and osteocalcin are expressed later as cells progress toward a mature, matrix-depositing osteoblastic phenotype. This suggests that incorporating AMP into the scaffold promotes a noticeable osteogenic differentiation response, even in a non-osseous environment, initiating early osteogenic commitment and ultimately leading to markers of matrix maturation and mineralization. Still, the subcutaneous implantation model does not fully reproduce the vascularized, anatomically confined, and immunologically dynamic environment of the dental pulp, particularly under inflammatory conditions. Thus, future studies employing pulp exposure models and direct comparison with standard materials will be valuable to further validate the translational potential of this bilayer scaffold.

4. Conclusion

This investigation demonstrates that a photocrosslinkable electrospun GelMA-based bilayer scaffold, comprising an ibuprofen-releasing layer and an amorphous magnesium phosphate layer, can concurrently suppress inflammation and promote the formation of mineralized tissue. It provides a rapid ibuprofen burst release followed by a 14-day sustained IBP presentation, which significantly reduces NF-κB activation and the pro-inflammatory cytokines IL-1α, TNF-α, and IL-6 in LPS-challenged macrophages. Meanwhile, the release of Mg^{2+} and PO_4^{3-} ions from AMP increases DPSC alkaline phosphatase activity, mineral deposition, and odontogenic gene transcription. In a three-dimensional, LPS-inflamed artificial pulp chamber, our novel bilayer scaffold decreased *IL1A*, *IL1B*, and *TNF* within 3 h and, after 14 days, increased the expression of *ALPL*, *DSPP*, and *OCN* compared to GelMA controls, confirming its ability to coordinate early immunomodulation with later mineralization signals. Ectopic rat implantation demonstrated biocompatibility, accelerated the macrophage M1/M2 transition, and showed expression of positive osteogenic markers indicative of progressing mineralization. In sum, our findings suggest that our bilayer scaffold represents a user-friendly device that shows potential for future clinical applications during vital pulp therapy.

CRediT authorship contribution statement

Caroline Anselmi: Writing – review & editing, Writing – original draft, Visualization, Validation, Project administration, Methodology, Investigation, Formal analysis, Data curation, Conceptualization. **Renan Dal-Fabbro:** Writing – review & editing, Methodology, Investigation, Formal analysis, Data curation. **Hisham Abada:** Writing – review & editing, Investigation, Formal analysis. **Igor Paulino Mendes Soares:** Writing – review & editing, Methodology, Investigation, Formal analysis. **Lais M. Cardoso:** Writing – review & editing, Methodology, Investigation, Formal analysis, Data curation. **Abdel H. Mahmoud:** Methodology, Investigation. **Julia C. Catalano:** Writing – review & editing, Methodology, Investigation. **Ana Beatriz Gomes de Carvalho:** Methodology, Investigation. **Yuanyuan Han:** Methodology, Investigation, Formal analysis. **Prabaha Sikder:** Writing – review & editing, Methodology, Investigation. **Anna Schwendeman:** Methodology, Investigation, Formal analysis. **Josimeri Hebling:** Writing – review & editing, Validation, Methodology, Investigation, Formal analysis. **Marco C. Bottino:** Writing – review & editing, Validation, Supervision, Resources, Project administration, Methodology, Funding acquisition, Conceptualization.

Acknowledgements

The authors thank the National Institutes of Health [NIH – National Institute of Dental and Craniofacial Research/NIDCR, grant R01DE031476 (M.C.B.) for financial support. The content is solely the responsibility of the authors and does not necessarily represent the official views of the National Institutes of Health.

Data availability

Data will be made available on request.

References

[1] J.C. Farges, B. Alliot-Licht, E. Renard, M. Ducret, A. Gaudin, A.J. Smith, P. R. Cooper, Dental pulp defence and repair mechanisms in dental caries, Mediators Inflamm. 2015 (2015) 230251, https://doi.org/10.1155/2015/230251.
[2] F. Iaculli, F.J. Rodriguez-Lozano, B. Briseno-Marroquin, T.G. Wolf, G. Spagnuolo, S. Rengo, Vital pulp therapy of permanent teeth with reversible or irreversible pulpitis: an overview of the literature, J. Clin. Med. 11 (14) (2022), https://doi.org/10.3390/jcm11144016.
[3] S. Cushley, H.F. Duncan, M.J. Lappin, P. Chua, A.D. Elamin, M. Clarke, I.A. El-Karim, Efficacy of direct pulp capping for management of cariously exposed pulps in permanent teeth: a systematic review and meta-analysis, Int. Endod. J. 54 (4) (2021) 556–571, https://doi.org/10.1111/iej.13449.
[4] D. Ricucci, I.N. Rocas, F.R.F. Alves, P.H. Cabello, J.F. Siqueira Jr., Outcome of direct pulp capping using calcium hydroxide: a long-term retrospective study, J Endod 49 (1) (2023) 45–54, https://doi.org/10.1016/j.joen.2022.11.005.

[5] C.A. de Souza Costa, P.T. Duarte, P.P. de Souza, E.M. Giro, J. Hebling, Cytotoxic effects and pulpal response caused by a mineral trioxide aggregate formulation and calcium hydroxide, Am. J. Dent. 21 (4) (2008) 255–261.
[6] D.H. Kim, J.H. Jang, B.N. Lee, H.S. Chang, I.N. Hwang, W.M. Oh, S.H. Kim, K. S. Min, J.T. Koh, Y.C. Hwang, Anti-inflammatory and mineralization effects of ProRoot MTA and endocem MTA in studies of human and rat dental pulps in vitro and in vivo, J. Endod. 44 (10) (2018) 1534–1541, https://doi.org/10.1016/j.joen.2018.07.012.
[7] AAE position statement on vital pulp therapy, J. Endod. 47 (9) (2021) 1340–1344, https://doi.org/10.1016/j.joen.2021.07.015.
[8] R. Dal-Fabbro, W.B. Swanson, L.C. Capalbo, H. Sasaki, M.C. Bottino, Next-generation biomaterials for dental pulp tissue immunomodulation, Dent. Mater. 39 (4) (2023) 333–349, https://doi.org/10.1016/j.dental.2023.03.013.
[9] S.N. Kaushik, B. Kim, A.M. Walma, S.C. Choi, H. Wu, J.J. Mao, H.W. Jun, K. Cheon, Biomimetic microenvironments for regenerative endodontics, Biomater. Res. 20 (2016) 14, https://doi.org/10.1186/s40824-016-0061-7.
[10] W.B. Swanson, A.H. Mahmoud, S. Woodbury, M.C. Bottino, Methacrylated gelatin as an on-demand injectable vehicle for drug delivery in dentistry, Methods Mol. Biol. 2588 (2023) 493–503, https://doi.org/10.1007/978-1-0716-2780-8_30.
[11] S.S. Namazi, A.H. Mahmoud, R. Dal-Fabbro, Y. Han, J. Xu, H. Sasaki, J.C. Fenno, M.C. Bottino, Multifunctional and biodegradable methacrylated gelatin/Aloe vera nanofibers for endodontic disinfection and immunomodulation, Biomater. Adv. 150 (2023) 213427, https://doi.org/10.1016/j.bioadv.2023.213427.
[12] A.A. Ayoub, A.H. Mahmoud, J.S. Ribeiro, A. Daghrery, J. Xu, J.C. Fenno, A. Schwendeman, H. Sasaki, R. Dal-Fabbro, M.C. Bottino, Electrospun azithromycin-laden gelatin Methacryloyl fibers for endodontic infection control, Int. J. Mol. Sci. 23 (22) (2022), https://doi.org/10.3390/ijms232213761.
[13] Y. Han, R. Dal-Fabbro, A.H. Mahmoud, M. Rahimnejad, J. Xu, M. Castilho, W. L. Dissanayaka, M.C. Bottino, GelMA/TCP nanocomposite scaffold for vital pulp therapy, Acta Biomater. 173 (2024) 495–508, https://doi.org/10.1016/j.actbio.2023.11.005.
[14] U. Klammert, A. Ignatius, U. Wolfram, T. Reuther, U. Gbureck, In vivo degradation of low temperature calcium and magnesium phosphate ceramics in a heterotopic model, Acta Biomater. 7 (9) (2011) 3469–3475, https://doi.org/10.1016/j.actbio.2011.05.022.
[15] H. Zhou, T.J. Luchini, S.B. Bhaduri, Microwave assisted synthesis of amorphous magnesium phosphate nanospheres, J. Mater. Sci. Mater. Med. 23 (12) (2012) 2831–2837, https://doi.org/10.1007/s10856-012-4743-y.
[16] M. Nabiyouni, Y. Ren, S.B. Bhaduri, Magnesium substitution in the structure of orthopedic nanoparticles: a comparison between amorphous magnesium phosphates, calcium magnesium phosphates, and hydroxyapatites, Mater. Sci. Eng. C 52 (2015) 11–17, https://doi.org/10.1016/j.msec.2015.03.032.
[17] M. Nabiyouni, T. Bruckner, H. Zhou, U. Gbureck, S.B. Bhaduri, Magnesium-based bioceramics in orthopedic applications, Acta Biomater. 66 (2018) 23–43, https://doi.org/10.1016/j.actbio.2017.11.033.
[18] N. Dubey, J.A. Ferreira, J. Malda, S.B. Bhaduri, M.C. Bottino, Extracellular matrix/amorphous magnesium phosphate bioink for 3D bioprinting of Craniomaxillofacial bone tissue, ACS Appl. Mater. Interfaces 12 (21) (2020) 23752–23763, https://doi.org/10.1021/acsami.0c05311.
[19] F.R. Ribeiro-Santos, M.F.M. Arnez, M.S. de Carvalho, R.A.B. da Silva, M.P.L. Politi, A.M. de Queiroz, P. Nelson-Filho, L.A.B. da Silva, L.H. Faccioli, F.W.G. Paula-Silva, Effect of non-steroidal anti-inflammatory drugs on pulpal and periapical inflammation induced by lipopolysaccharide, Clin. Oral Investig. 25 (11) (2021) 6201–6209, https://doi.org/10.1007/s00784-021-03919-3.
[20] H. Abukawa, M. Phelps, P. Jackson, R.M. Smith, J.P. Vacanti, L.B. Kaban, M. J. Troulis, Effect of ibuprofen on osteoblast differentiation of porcine bone marrow-derived progenitor cells, J. Oral Maxillofac. Surg. 67 (11) (2009) 2412–2417, https://doi.org/10.1016/j.joms.2009.05.434.
[21] H. Salkin, K.E. Basaran, Effects of non-steroidal anti-inflammatory drug (ibuprofen) in low and high dose on stemness and biological characteristics of human dental pulp-derived mesenchymal stem cells, Connect. Tissue Res. 64 (1) (2023) 14–25, https://doi.org/10.1080/03008207.2022.2083613.
[22] T.A. Jeckson, Y.P. Neo, S.P. Sisinthy, B. Gorain, Delivery of therapeutics from layer-by-layer electrospun nanofiber matrix for wound healing: an update, J. Pharm. Sci. 110 (2) (2021) 635–653, https://doi.org/10.1016/j.xphs.2020.10.003.
[23] L.M. Cardoso, A.B.G. de Carvalho, C. Anselmi, A.H. Mahmoud, R. Dal-Fabbro, F. G. Basso, M.C. Bottino, Bifunctional naringenin-laden gelatin methacryloyl scaffolds with osteogenic and anti-inflammatory properties, Dent. Mater. (2024), https://doi.org/10.1016/j.dental.2024.06.019.
[24] C. Anselmi, I.P. Mendes Soares, S. Chang, L.M. Cardoso, A.B.G. de Carvalho, R. Dal-Fabbro, C.A. de Souza Costa, M.C. Bottino, J. Hebling, Quercetin-calcium hydroxide scaffolds modulate dental pulp stem cell response in vitro under a simulated inflammatory environment, Int. Endod. J. 58 (7) (2025) 1073–1090, https://doi.org/10.1111/iej.14243.
[25] I.P. Mendes Soares, C. Anselmi, M. Pires, R.A.O. Ribeiro, M.L. Leite, D.G. Soares, J. Hebling, Chronic exposure to lipopolysaccharides as an in vitro model to simulate the impaired odontogenic potential of dental pulp cells under pulpitis conditions, J. Appl. Oral Sci. 31 (2023) e20230032, https://doi.org/10.1590/1678-7757-2023-0032.
[26] A. Daghrery, R. Dal-Fabbro, J. Xu, D. Kaigler, M. de Ruijter, D. Gawlitta, J. Malda, M.C. Bottino, Niche-inspired collagen infused melt electrowritten scaffolds for craniofacial bone regeneration, Biomater. Adv. 170 (2025) 214222, https://doi.org/10.1016/j.bioadv.2025.214222.
[27] J.R. de Souza, C. Anselmi, L.M. Cardoso, L.T. Kito, A.H. Dos Reis-Prado, P.H.C. de Oliveira, R. Dal-Fabbro, M. Rahimnejad, T.M.B. Campos, L.T.A. Cintra, A.L. S. Borges, M.C. Bottino, Electrospun SilkMA/silicate-chlorinated cobalt-doped bioactive glass composite for bone regeneration, J. Mech. Behav. Biomed. Mater. 164 (2025) 106929, https://doi.org/10.1016/j.jmbbm.2025.106929.
[28] A.H. Mahmoud, Y. Han, R. Dal-Fabbro, A. Daghrery, J. Xu, D. Kaigler, S.B. Bhaduri, J. Malda, M.C. Bottino, Nanoscale beta-TCP-laden GelMA/PCL composite membrane for guided bone regeneration, ACS Appl. Mater. Interfaces 15 (27) (2023) 32121–32135, https://doi.org/10.1021/acsami.3c03059.
[29] M. Ahmadi Bonakdar, D. Rodrigue, Electrospinning: processes, structures, and materials, Macromol 4 (1) (2024) 58–103.
[30] P. Sikder, J.A. Ferreira, E.A. Fakhrabadi, K.Z. Kantorski, M.W. Liberatore, M. C. Bottino, S.B. Bhaduri, Bioactive amorphous magnesium phosphate-polyetheretherketone composite filaments for 3D printing, Dent. Mater. 36 (7) (2020) 865–883, https://doi.org/10.1016/j.dental.2020.04.008.
[31] A. Wahab, G.M. Khan, M. Akhlaq, N. Khan, A. Hussain, Pre-formulation investigation and in vitro evaluation of directly compressed ibuprofen-ethocel oral controlled release matrix tablets: a kinetic approach, Afr. J. Pharm. Pharmacol 5 (2011) 2118–2127, https://doi.org/10.5897/AJPP11.128.
[32] A.V. Ewing, G.S. Clarke, S.G. Kazarian, Attenuated total reflection-Fourier transform infrared spectroscopic imaging of pharmaceuticals in microfluidic devices, Biomicrofluidics 10 (2) (2016) 024125, https://doi.org/10.1063/1.4946867.
[33] S.F. Chou, K.A. Woodrow, Relationships between mechanical properties and drug release from electrospun fibers of PCL and PLGA blends, J. Mech. Behav. Biomed. Mater. 65 (2017) 724–733, https://doi.org/10.1016/j.jmbbm.2016.09.004.
[34] B. Ozcan, E. Bayrak, C. Erisken, Characterization of human dental pulp tissue under oscillatory shear and compression, J. Biomech. Eng. 138 (6) (2016) 061006, https://doi.org/10.1115/1.4033437.
[35] V. Rosa, B.N. Cavalcanti, J.E. Nor, A. Tezvergil-Mutluay, N. Silikas, M.C. Bottino, A. Kishen, D.G. Soares, C.M. Franca, P.R. Cooper, H.F. Duncan, J.L. Ferracane, D. C. Watts, Guidance for evaluating biomaterials' properties and biological potential for dental pulp tissue engineering and regeneration research, Dent. Mater. 41 (3) (2025) 248–264, https://doi.org/10.1016/j.dental.2024.12.003.
[36] P. Noohi, M.J. Abdekhodaie, M.H. Nekoofar, K.M. Galler, P.M.H. Dummer, Advances in scaffolds used for pulp-dentine complex tissue engineering: a narrative review, Int. Endod. J. 55 (12) (2022) 1277–1316, https://doi.org/10.1111/iej.13826.
[37] R. Teimouri, K. Abnous, S.M. Taghdisi, M. Ramezani, M. Alibolandi, Surface modifications of scaffolds for bone regeneration, J. Mater. Res. Technol. 24 (2023) 7938–7973, https://doi.org/10.1016/j.jmrt.2023.05.076.
[38] A. Silverberg, L.M. Cardoso, A.B.G. de Carvalho, A.H. dos Reis-Prado, J.C. Fenno, R. Dal-Fabbro, M.C. Bottino, Metronidazole-laden silk fibroin methacrylated scaffolds for managing periapical lesions, Odontology (2024), https://doi.org/10.1007/s10266-024-01023-y.
[39] K. Yoshiba, N. Yoshiba, H. Nakamura, M. Iwaku, H. Ozawa, Immunolocalization of fibronectin during reparative dentinogenesis in human teeth after pulp capping with calcium hydroxide, J. Dent. Res. 75 (8) (1996) 1590–1597, https://doi.org/10.1177/00220345960750081101.
[40] T. Giraud, C. Jeanneau, C. Rombouts, H. Bakhtiar, P. Laurent, I. About, Pulp capping materials modulate the balance between inflammation and regeneration, Dent. Mater. 35 (1) (2019) 24–35, https://doi.org/10.1016/j.dental.2018.09.008.
[41] P.I. Lee, Kinetics of drug release from hydrogel matrices, J. Control. Release 2 (1985) 277–288, https://doi.org/10.1016/0168-3659(85)90051-3.
[42] D.M. Alshangiti, T.K. El-damhougy, A. Zaher, M. Madani, M., Mohamady ghobashy, revolutionizing biomedicine: advancements, applications, and prospects of nanocomposite macromolecular carbohydrate-based hydrogel biomaterials: a review, RSC, Advances 13 (50) (2023) 35251–35291, https://doi.org/10.1039/D3RA07391B.
[43] Z. Wang, H. Lv, H. Du, S. Liu, L. Huang, Z. Pan, W. Xie, M. Yang, S. Chen, L. Liu, H. Pan, D. Li, H. Sun, Dual scalable osteogenic microtissue engineering via GelMA microsphere-inspired mechanical training and autonomous assembling of dental pulp stem cell, Int. J. Biol. Macromol. 282 (Pt 1) (2024) 136258, https://doi.org/10.1016/j.ijbiomac.2024.136258.
[44] S. Buyuksungur, V. Hasirci, N. Hasirci, 3D printed hybrid bone constructs of PCL and dental pulp stem cells loaded GelMA, J. Biomed. Mater. Res. A 109 (12) (2021) 2425–2437, https://doi.org/10.1002/jbm.a.37235.
[45] S. Aminmansour, A.B. Gomes de Carvalho, L. Medeiros Cardoso, C. Anselmi, M. Rahimnejad, R. Dal-Fabbro, E. Benavides, T.M.B. Campos, A.L.S. Borges, M. C. Bottino, Strontium-doped bioglass-laden gelatin Methacryloyl hydrogels for vital pulp therapy, J. Funct. Biomater. 15 (4) (2024), https://doi.org/10.3390/jfb15040105.
[46] W. Wang, Y. Zhu, Y. Liu, B. Chen, M. Li, C. Yuan, P. Wang, 3D bioprinting of DPSCs with GelMA hydrogel of various concentrations for bone regeneration, Tissue Cell 88 (2024) 102418, https://doi.org/10.1016/j.tice.2024.102418.
[47] P. Paymanpour, C. Anselmi, L.M. Cardoso, A.B.G. de Carvalho, I.P.M. Soares, J. Hebling, R. Dal-Fabbro, M.C. Bottino, Anti-inflammatory potential of casein enzymatic hydrolysate/gelatin methacryloyl scaffolds for vital pulp therapy, Clin. Oral Investig. 28 (9) (2024), https://doi.org/10.1007/s00784-024-05877-y.
[48] A. Khayat, N. Monteiro, E.E. Smith, S. Pagni, W. Zhang, A. Khademhosseini, P. C. Yelick, GelMA-encapsulated hDPSCs and HUVECs for dental pulp regeneration, J. Dent. Res. 96 (2) (2017) 192–199, https://doi.org/10.1177/0022034516682005.
[49] R. Diana, R. Ardhani, Y. Kristanti, P. Santosa, Dental pulp stem cells response on the nanotopography of scaffold to regenerate dentin-pulp complex tissue, Regen. Ther. 15 (2020) 243–250, https://doi.org/10.1016/j.reth.2020.09.007.
[50] J. Wang, H. Ma, X. Jin, J. Hu, X. Liu, L. Ni, P.X. Ma, The effect of scaffold architecture on odontogenic differentiation of human dental pulp stem cells,

Biomaterials 32 (31) (2011) 7822–7830, https://doi.org/10.1016/j.biomaterials.2011.04.034.
[51] S. Hasegawa, T. Ichiyama, F. Kohno, Y. Korenaga, A. Ohsaki, R. Hirano, Y. Haneda, R. Fukano, S. Furukawa, Prostaglandin E2 suppresses beta1-integrin expression via E-prostanoid receptor in human monocytes/macrophages, Cell. Immunol. 263 (2) (2010) 161–165, https://doi.org/10.1016/j.cellimm.2010.03.010.
[52] X. Bai, J. Wang, L. Zhang, J. Ma, H. Zhang, S. Xia, M. Zhang, X. Ma, Y. Guo, R. Rong, S. Cheng, W. Shu, Y. Wang, J. Leng, Prostaglandin E(2) receptor EP1-mediated phosphorylation of focal adhesion kinase enhances cell adhesion and migration in hepatocellular carcinoma cells, Int. J. Oncol. 42 (5) (2013) 1833–1841, https://doi.org/10.3892/ijo.2013.1859.
[53] J. Zhang, X. Ma, D. Lin, H. Shi, Y. Yuan, W. Tang, H. Zhou, H. Guo, J. Qian, C. Liu, Magnesium modification of a calcium phosphate cement alters bone marrow stromal cell behavior via an integrin-mediated mechanism, Biomaterials 53 (2015) 251–264, https://doi.org/10.1016/j.biomaterials.2015.02.097.
[54] M. Shimaya, T. Muneta, S. Ichinose, K. Tsuji, I. Sekiya, Magnesium enhances adherence and cartilage formation of synovial mesenchymal stem cells through integrins, Osteoarthr. Cartil. 18 (10) (2010) 1300–1309, https://doi.org/10.1016/j.joca.2010.06.005.
[55] M. Takeichi, T.S. Okada, Roles of magnesium and calcium ions in cell-to-substrate adhesion, Exp. Cell Res. 74 (1) (1972) 51–60, https://doi.org/10.1016/0014-4827(72)90480-6.
[56] H. Rubin, Magnesium: the missing element in molecular views of cell proliferation control, Bioessays 27 (3) (2005) 311–320, https://doi.org/10.1002/bies.20183.
[57] C. Cappadone, E. Malucelli, M. Zini, G. Farruggia, G. Picone, A. Gianoncelli, A. Notargiacomo, M. Fratini, C. Pignatti, S. Iotti, C. Stefanelli, Assessment and imaging of intracellular magnesium in SaOS-2 osteosarcoma cells and its role in proliferation, Nutrients 13 (4) (2021), https://doi.org/10.3390/nu13041376.
[58] R.W. Li, N.T. Kirkland, J. Truong, J. Wang, P.N. Smith, N. Birbilis, D.R. Nisbet, The influence of biodegradable magnesium alloys on the osteogenic differentiation of human mesenchymal stem cells, J. Biomed. Mater. Res. A 102 (12) (2014) 4346–4357, https://doi.org/10.1002/jbm.a.35111.
[59] C.A. de Souza Costa, J. Hebling, D.L. Scheffel, D.G. Soares, F.G. Basso, A.P. Ribeiro, Methods to evaluate and strategies to improve the biocompatibility of dental materials and operative techniques, Dent. Mater. 30 (7) (2014) 769–784, https://doi.org/10.1016/j.dental.2014.04.010.
[60] D.G. Soares, E.A.F. Bordini, W.B. Swanson, C.A. de Souza Costa, M.C. Bottino, Platform technologies for regenerative endodontics from multifunctional biomaterials to tooth-on-a-chip strategies, Clin. Oral Investig. 25 (8) (2021) 4749–4779, https://doi.org/10.1007/s00784-021-04013-4.
[61] A. Adamickova, J. Kyselovic, M. Adamicka, N. Chomanicova, S. Valaskova, B. Salingova, M. Molitorisova, Z. Cervenak, L. Danisovic, A. Gazova, Effects of ibuprofen and diclofenac pre-treatment on viability and apoptosis processes in human dental pulp stem cells, Medicina (Kaunas) 60 (5) (2024), https://doi.org/10.3390/medicina60050787.
[62] M. Muller, O. Raabe, K. Addicks, S. Wenisch, S. Arnhold, Effects of non-steroidal anti-inflammatory drugs on proliferation, differentiation and migration in equine mesenchymal stem cells, Cell Biol. Int. 35 (3) (2011) 235–248, https://doi.org/10.1042/CBI20090211.
[63] P.R. Cooper, M.J. Holder, A.J. Smith, Inflammation and regeneration in the dentin-pulp complex: a double-edged sword, J. Endod. 40 (4 Suppl) (2014) S46–S51, https://doi.org/10.1016/j.joen.2014.01.021.
[64] V. Hirsch, M. Wolgin, A.V. Mitronin, A.M. Kielbassa, Inflammatory cytokines in normal and irreversibly inflamed pulps: a systematic review, Arch. Oral Biol. 82 (2017) 38–46, https://doi.org/10.1016/j.archoralbio.2017.05.008.
[65] K. Kritikou, M. Greabu, M. Imre, D. Miricescu, A. Ripszky Totan, M. Burcea, S. Stanescu II, T. Spinu, ILs and MMPs levels in inflamed human dental pulp: a systematic review, Molecules 26 (14) (2021), https://doi.org/10.3390/molecules26144129.
[66] A. Brodzikowska, M. Ciechanowska, M. Kopka, A. Stachura, P.K. Wlodarski, Role of lipopolysaccharide, derived from various bacterial species, in pulpitis-a systematic review, Biomolecules 12 (1) (2022), https://doi.org/10.3390/biom12010138.
[67] S.T. Palayoor, M.Y. Youmell, S.K. Calderwood, C.N. Coleman, B.D. Price, Constitutive activation of IkappaB kinase alpha and NF-kappaB in prostate cancer cells is inhibited by ibuprofen, Oncogene 18 (51) (1999) 7389–7394, https://doi.org/10.1038/sj.onc.1203160.
[68] N. Scheuren, H. Bang, T. Munster, K. Brune, A. Pahl, Modulation of transcription factor NF-kappaB by enantiomers of the nonsteroidal drug ibuprofen, Br. J. Pharmacol. 123 (4) (1998) 645–652, https://doi.org/10.1038/sj.bjp.0701652.
[69] Z. Xie, S. Tang, G. Ye, P. Wang, J. Li, W. Liu, M. Li, S. Wang, X. Wu, S. Cen, G. Zheng, M. Ma, Y. Wu, H. Shen, Interleukin-6/interleukin-6 receptor complex promotes osteogenic differentiation of bone marrow-derived mesenchymal stem cells, Stem Cell Res. Ther. 9 (1) (2018) 13, https://doi.org/10.1186/s13287-017-0766-0.
[70] A. Bernad, M. Kopf, R. Kulbacki, N. Weich, G. Koehler, J.C. Gutierrez-Ramos, Interleukin-6 is required in vivo for the regulation of stem cells and committed progenitors of the hematopoietic system, Immunity 1 (9) (1994) 725–731, https://doi.org/10.1016/s1074-7613(94)80014-6.
[71] M. Chung, S. Lee, S. Kim, E. Kim, Inflammatory response and odontogenic differentiation of inflamed dental pulp treated with different pulp capping materials: an in vivo study, Int. Endod. J. (2023), https://doi.org/10.1111/iej.13947.
[72] R. Hoseinifar, A. Eskandarizadeh, M. Parirokh, M. Torabi, F. Safarian, E. Rahmanian, Histologic evaluation of human pulp response to capping with Mta, Cem cement and biodentine, J. Dent. 21 (3) (2020) 177–183, https://doi.org/10.30476/dentjods.2019.81796.0.
[73] U. Schroder, Effects of calcium hydroxide-containing pulp-capping agents on pulp cell migration, proliferation, and differentiation, J. Dent. Res. (1985) 541–548, https://doi.org/10.1177/00220345850640407, 64 Spec No.
[74] N. Moore, C. Pollack, P. Butkerait, Adverse drug reactions and drug-drug interactions with over-the-counter NSAIDs, Ther. Clin. Risk Manag. 11 (2015) 1061–1075, https://doi.org/10.2147/tcrm.S79135.
[75] F. Pahlevanzadeh, R. Emadi, M. Setayeshmehr, M. Kharaziha, S.A. Poursamar, Antibacterial amorphous magnesium phosphate/graphene oxide for accelerating bone regeneration, Biomater. Adv. 138 (2022) 212856, https://doi.org/10.1016/j.bioadv.2022.212856.
[76] Y. Lu, L. Ye, S. Yu, S. Zhang, Y. Xie, M.D. McKee, Y.C. Li, J. Kong, J.D. Eick, S. L. Dallas, J.Q. Feng, Rescue of odontogenesis in Dmp1-deficient mice by targeted re-expression of DMP1 reveals roles for DMP1 in early odontogenesis and dentin apposition in vivo, Dev. Biol. 303 (1) (2007) 191–201, https://doi.org/10.1016/j.ydbio.2006.11.001.
[77] A.R. Donaldson, C.E. Tanase, D. Awuah, P. Vasanthi Bathrinarayanan, L. Hall, M. Nikkhah, A. Khademhosseini, F. Rose, C. Alexander, A.M. Ghaemmaghami, Photocrosslinkable gelatin hydrogels modulate the production of the major pro-inflammatory cytokine, TNF-alpha, by human mononuclear cells, Front. Bioeng. Biotechnol. 6 (2018) 116, https://doi.org/10.3389/fbioe.2018.00116.
[78] J. Hao, B. Zou, K. Narayanan, A. George, Differential expression patterns of the dentin matrix proteins during mineralized tissue formation, Bone 34 (6) (2004) 921–932, https://doi.org/10.1016/j.bone.2004.01.020.
[79] R. Dal-Fabbro, C. Anselmi, W.B. Swanson, L. Medeiros Cardoso, P.T.A. Toledo, A. Daghrery, D. Kaigler, A. Abel, M.L. Becker, S. Soliman, M.C. Bottino, Amino acid-based poly(ester urea) biodegradable membrane for guided bone regeneration, ACS Appl. Mater. Interfaces (2024), https://doi.org/10.1021/acsami.4c09742.
[80] M.S. Álvarez, L. Mazzei, M.B. Hapon, I. Quesada, L. Salvarredi, D. Beltramo, C. Castro, New formulation of ibuprofen-arginate reduces oxidative stress and prevents macrophage polarization toward M1 phenotype, Biomed. Pharmacother. 183 (2025) 117819, https://doi.org/10.1016/j.biopha.2025.117819.
[81] P.-H. Wang, Y. Wang, Y.-Y. Guo, Z.-H. Ma, C. Wu, L. Xing, Ibuprofen modulates macrophage polarization by downregulating poly (ADP-ribose) polymerase 1, Int. Immunopharmacol. 143 (2024) 113502, https://doi.org/10.1016/j.intimp.2024.113502.
[82] L. Yan, J. Wang, X. Cai, Y.-C. Liou, H.-M. Shen, J. Hao, C. Huang, G. Luo, W. He, Macrophage plasticity: signaling pathways, tissue repair, and regeneration, MedComm 5 (8) (2024) e658, https://doi.org/10.1002/mco2.658.
[83] Y. Yu, Z. Yue, M. Xu, M. Zhang, X. Shen, Z. Ma, J. Li, X. Xie, Macrophages play a key role in tissue repair and regeneration, PeerJ 10 (2022) e14053, https://doi.org/10.7717/peerj.14053.